

Chapter 18

HRMA Ring Focus Measurements

Ping Zhao

18.1 Introduction

The HRMA ring focus measurement is an essential part of the AXAF ground calibration. It allows diagnosis of features not evident in the focal plane.

During the calibration, the HRMA was mounted horizontally. Because each of the eight mirror shells was bonded with epoxy to 12 invar pads around outside of the shell, the shells were distorted by small but measurable amounts by the mechanical support system due to gravity, thermal effects, and strain in the epoxy bonds. Furthermore, the moisture gain or loss in the epoxy bond (as it cures) changes the thickness of the epoxy bonds, and therefore causes the mirror distortions vary with time.

To ensure a scientifically successful mission and to predict the AXAF on-orbit performance, these distortions need to be measured carefully and their impact needs to be assessed. For example, the gravity distortion needs to be removed and the epoxy strain and its change with time needs to be evaluated for on-orbit performance predictions.

The HRMA ring focus measurements were designed and carried out for the above purpose. The ring focus is a sharply focused ring formed by the X-rays before they reach the HRMA focal plane (Griner et al., 1985; Zissa and Korsch, 1986). It is caused by spherical aberrations due to the finite source distance at the XRCF. There are four rings, one for each of the four shells of the HRMA.

The HRMA ring focus measurements were made with a High Speed Imager (HSI)¹ and a High Resolution Camera (HRC)², both microchannel plate X-ray detectors. The measurements reveal aspects of the mirror surface figures and distortions which are difficult or impossible to detect in the focal plane. The measurement results show periodic modulations of the ring width which were caused by gravity and strain in the epoxy bonds. The strongest component of the modulation has 12-fold symmetry due to the 12 flexures that support each mirror shell. Five ring focus HSI images and one HRC images were taken at different energies during the HRMA calibration (from 1996/12/20 to 1997/04/10). By examining the small changes in the ring width, temporal effects (such as changes in epoxy strain) can be diagnosed.

¹The High Speed Imager (HSI) is part of the HRMA X-ray Detection System (HXDS).

²The High Resolution Camera (HRC) is one of the two AXAF detectors, P.I.: S. Murray(Murray et al., 1997).

The HRMA ring focus measurements were planned because of the success of similar measurements done for the VETA-I (Verification Engineering Test Article I) experiment in 1991 (Zhao et al., 1993). The data analysis here is based on that described in Zhao et al. (1993).

In this chapter we discuss the ring focus measurement results, ring focus model, the epoxy strain issue and its effect on the HRMA on-orbit performance. In §18.2 we describe the ring focus measurements and the data obtained. In §18.3 we discuss the data analysis. In §18.4 we present the measurement results with figures. In §18.5 we describe the ring focus models. In §18.6 we compare the data with the models. Finally, in §18.7 we summarize the ring focus measurements, our current assessment to the HRMA mirror deformation, evaluate the epoxy strain change between the ground calibration and on-orbit, and discuss the impact on the HRMA on-orbit performance.

18.2 Measurements and Data

Based on raytrace simulations, the ring focus plane was calculated to be 65.2 mm towards the HRMA from the focal plane (or 10209.3 mm from the CAP datum A – front surface of the Central Aperture Plate). The ring focus measurements were made in this plane. Five long exposure (1800 seconds) images were taken between 1996/12/23 and 1997/02/10 with an HSI detector. Then two months later, on 1997/04/10, an HRC image was taken with 6000 second integration time. Table 18.1 lists these six ring focus images. There was a repress (the test vacuum chamber was repressurized and opened) between the first and the second ring focus measurements, another repress between the fourth and the fifth measurements, and two represses between the fifth and the sixth measurements. Work was done on the HRMA alignment mechanism (actuators) during the first two repress cycles.

Table 18.1: HRMA Ring Focus Measurement data

Date (GMT)	Run ID	TRW ID	Source	Defocus	Detector	Integration time
961223	106856	C-IXH-RF-1.005	Al-K	65.2 mm	HSI	1800 seconds
970110	108185	D-IXH-RF-1.003	Fe-K	65.2 mm	HSI	1800 seconds
970115	108944	D-IXH-RF-1.002	C-K	65.2 mm	HSI	1800 seconds
970124	110004	D-IXH-RF-1.005	Al-K	65.2 mm	HSI	1800 seconds
970210	111804	E-IXH-RF-1.007	Al-K	65.2 mm	HSI	1800 seconds
970410	114828	G-IHI-RF-7.007	Mg-K	65.2 mm	HRC	6000 seconds

Figures 18.1 through 18.6 show these six ring focus images. Four rings in each figure are X-ray images from the four mirror shells of the HRMA. The images shown are as seen from the mirror looking towards the focal plane – top is the top, bottom is the bottom, left is the north and right is the south of the XRCF. The 12 gaps around the rings are the shadows of the supporting struts in the apertures and collimators.³ A scale bar at the bottom of each figure shows the size of 1 mm or 20.2". At the 65.2 mm defocus, the mean radii of the four rings are 3.88 mm, 3.10 mm, 2.73 mm, and 2.05 mm for shells 1,3,4, and 6, respectively.

In the five HSI images, the right (south) sides of the images are brighter than the left. This is because the HSI quantum efficiency is a function of incident angle; the HSI pores were tilted about

³From the 12 gap positions, it was found that the orientation of the HSI was slightly misaligned with respect to the HRMA (the HSI was rotated 0.7° clockwise, so the HRMA images appeared on the HSI were rotated 0.7° counterclockwise). This misalignment was considered in the data analysis.

6° from the detector normal, and about 10° below the south.⁴ In the HRC image this effect is not noticeable as the HRC quantum efficiency is not strongly dependent on the incident angle.

Near the 12 gaps of each ring, the ring width bulges out. This is primarily due to the effect of gravity induced distortions from the 12 mirror holders at those locations; we will discuss this later. In Figure 18.2, ring 1 (the largest ring) is very faint. This is because it is an Fe-K (6.4 keV) image. At this energy, the critical angle of reflection for Ir is 45.3 arcmin, while mirror P1 has a mean grazing angle of about 55.1 arcmin at the XRCF. This is beyond the critical angle, so there is not much reflection at 6.4 keV from shell 1. (The same is true for on-orbit operation, where shell 1 has a mean grazing angle of 51.3 arcmin.)

18.3 Data Analysis

Both HSI and HRC ring focus image data were digitized to a qpoe format in a 4096×4096 readout array with pixel size of $(6.43\mu\text{m})^2$. HSI has a spatial resolution of $\sim 14\mu\text{m}$ (FWHM) and HRC has a spatial resolution of $\sim 20\mu\text{m}$ (FWHM). Each image collected 1–2 million photons. Before the data analysis, the images were processed to remove artifacts. One of the processes is called degap. The image readout is a crossed grid charge detector, which consists of two orthogonal planes of wires electrically separated from each other. These two wire plates are located behind the microchannel plate stack to collect the charge. The electron charge cloud has a core/halo type of structure and spreads over several wires. A fine position algorithm was developed to determine the centroid of the charge cloud to a small fraction of the wire spacing. An artifact due to this algorithm is 16 vertical and 16 horizontal gaps left in the raw images (Chappell and Murray, 1989). The degap process restores the image so that each pixel appears at its actual location. By examining the final images, the residual gaps or pixel overlaps were determined to be less than one pixel wide.

Each degapped ring image was divided into annuli and pie sectors, using IRAF (Image Reduction and Analysis Facility). Each ring image was divided into annuli of one pixel ($6.43\mu\text{m}$) wide. Each sector was chosen to be 2° wide, which gives adequate statistical errors and azimuthal resolution. Photon counts in each cell of the annulus-sector grid were tabulated. Radial profiles across each ring for each azimuthal angle were plotted; Figures 18.7–18.10 show some ring profile examples. For most parts of the ring, the radial profiles are single peaked. Near the 12 gaps (except the top and the bottom gap), the radial profiles are double or even triple-peaked. This is because the mirror was slightly deformed at the 12 support points due to gravity (see §18.5).

The ring width RMS and FWHM, and the ring mean radius were calculated for each radial profile.⁵ There are a large number of scattered photons in each image. Because a photon far from the ring can carry a large statistical weight, the above calculations are meaningless without clipping. Therefore, a window of $320\mu\text{m}$ was set around each ring before performing the calculations. Inside this window, focused photons were overwhelmingly dominant over the scattered photons. Photons outside this window were scattered photons and therefore were ignored.

The ring width RMS was chosen to represent the ring width because it carries a better statistical value than the FWHM.⁶ The ring radii were affected by the detector plate scale non-uniformity, which is not very well known. Hence the ring radii are not analyzed here.

⁴From the ring focus data, the relative HSI quantum efficiency curve can be obtained since the X-ray incident angle can be very precisely determined and varies around the ring (see Chapter 7)

⁵The incident-angle-dependent QE of the HSI and HRC does not affect the values of RMS, FWHM, or the ring mean radius, although it does affect the errors as the number of detected photons varies. Different energies (except Fe-K) also should not affect these values as the analysis only use the focused rays.

⁶The RMS is calculated from all the data points within the window, while the FWHM is only based on three points.

18.4 Results

For each of the six images, the ring width RMS variation for each ring was plotted as a function of the azimuthal angle. Figures 18.11–18.14 show the ring width RMS variations for the image with run ID 110004. The top panels show the data points with error bars (the RMS calculated from those 180 angular sector profiles but with the data falling into the 12 gaps removed) as a function of the azimuthal angle, where 0° is at the top of the ring; 90° is to the south; 180° is at the bottom; and –90° is to the north. A modulation with a 30° period is clearly shown in this figure. Each middle panel is a spline fit to the data. Each bottom panel is the Fourier transformation of the data, plotted as the modulation power vs. the frequency in one circumference. The modulation has dominant frequencies of 2 (180° period), 12 (30° period) and its higher harmonics.

Figures 18.15–18.18 are the summary figures for the HRMA ring focus measurements. They show the ring width RMS variations and their Fourier transforms for all four rings from all six measurements. The six ring focus measurements were made over a time span of 3.5 months during the calibration. The purpose was to see if there were any changes with time in the ring structure, especially the 12 fold symmetry, in order to determine the change in the epoxy strain.

Rings with the Fe-K source (the dotted curve) have greater width because Fe-K has higher energy (6.4 keV), and therefore more scattering, which broadens the rings. Ring 1 for Fe-K is especially wide and noisy. This is because there were not many photons in ring 1 as mentioned before (see Figure 18.2). For shells 3, 4 and 6, the Fe-K rings are broader but basically match the profiles from other sources.

Data taken with Al-K and C-K source have enough counts and less scattering. They are used to do the comparison for the epoxy strain effect.

All the curves have 12 dominant split peaks at 30° multiples. They are primarily due to the gravity, and possibly also thermal, and epoxy strain effects. Since each shell was held at 12 rather small areas (the largest shells were epoxy bonded to 2 inch diameter invar pads), gravity caused local distortions at those 12 locations. The distortions along the sides of the mirror were more severe than at the top or bottom. These local distortions would cause a shifted 12-fold symmetry (i.e. 12 ± 1 and 12 ± 2 fold) and higher harmonics (i.e. 24 , 24 ± 1 and 24 ± 2 fold). A 2-fold symmetry also exists due to the fact that the amplitude of the side distortions are much larger than that from the top and bottom. The 2-fold symmetry is slightly upset because the epoxy gaps are not uniform at each of the 12 bonds.

18.5 Ring Focus Models

To understand the results of the HRMA ring focus measurements, we developed ring focus models. The ring focus models are computer generated images obtained by ray-tracing to simulate the X-rays passing through the HRMA mirror and the test system. Details such as scattering due to mirror surface roughness and the detector response were also simulated. The same analysis used for the real data was applied to the model images. As an example, Figure 18.19 is a HRMA model ring focus image with the epoxy strain set at –0.35% (i.e. an inward bump of 0.35% of the epoxy thickness at the bonding points; see below).

The ring focus models include the following elements:

1. HRMA mirror surface map from the HDOS.
2. HRMA mirror assembly errors as deduced from the EKC HATS data.
3. HRMA decenters and tilts as measured during the HRMA calibration at the XRCF.

4. Gravity (1-g) distortions modeled by SAO.
5. Epoxy strain distortions modeled by SAO.
6. Thermal effects.
7. Finite source distance.
8. HRMA apertures and their supporting struts.
9. HRMA mirror reflectivity and scattering due to surface micro-roughness.
10. HSI and HRC detector resolutions.

The HRMA mirror surface (low frequency) maps are from data obtained from the Hughes Danbury Optical Systems, Inc. (HDOS) metrology measurements. The HRMA mirror assembly errors were deduced from data obtained from the Eastman Kodak Company (EKC). Because mirror shells were made slightly different from ideal shells, they had to be bonded slightly different from the design positions in order to obtain the best on-orbit parfocalization. The HRMA decenter and tilt errors (H shells with respect to P shells) errors were measured and analyzed during the calibration (Gaetz et al., 1997).

The SAO 1-g model is a full 360 degree Finite Element Analysis (FEA) model. Twelve tangential flexures support each optic. In a 1-g vertical field, the FEA model shows that the flexures at the sides of the optic each support about 17% of the optic's weight, the flexures 30° above and below the sides support about 12% of the optic's weight and the flexures 60° above and below the sides support about 4% of the optic's weight. The flexures at the top and bottom support essentially no weight because of their flexibility. The flexures that are more highly loaded cause the optic to twist more about the optical axis (producing a so-called circumferential slope). At the side locations ($\pm 90^\circ$), the gravity causes a large slope change on the optic across the centerline of the flexure such that optic above the $\pm 90^\circ$ was pushed in while below the $\pm 90^\circ$ was pulled out. The peak-to-valley distortion ($\pm 85^\circ$ to $\pm 95^\circ$) was about $0.37\mu\text{m}$. Therefore there are inward dimples centered at around $\pm 85^\circ$ and outward dimples centered at around $\pm 95^\circ$. At the 30° above and below the side locations, the slope change is about 1/2 of that occurs at the side locations. At the 60° above and below, the slope change is about 1/6 of that. At the top and bottom of the optic, there is essentially no slope change as there is no twisting effect by the gravity. A more detailed analysis of the SAO 1-g model can be found in SAO memo by L.M. Cohen (Cohen, 1997).

The epoxy strain was measured on test flats at EKC. The results show two kinds of effects: (1) An in-plane cure shrinkage of about 0.075% and a "through-the-thickness" (TTT, through the 0.0075" nominal thickness direction) shrinkage of about 2% took place within a few days after bonding; (2) Long term epoxy strains of order 1% due to moisture gain and loss in the epoxy, -1% (inward bump) in the fully dried condition and +1% (outward bump) in the fully moist. For effect (1), we assume that about 1 week after each optic is bonded, there were 12 outward bumps. Those outward bumps were due to the large (-2%) TTT strain which causes the optic to be pulled outward while the flexure is pulled inward. The magnitude of this outward bump is the equivalent to an epoxy moisture strain of about +0.32%. For the effect (2), the epoxy strain will change based on the moisture. The time constant for this effect is order of months. A more detailed analysis of the epoxy strain effects can be found in SAO memo by L.M. Cohen (Cohen, 1997).

For the thermal effects, a uniform temperature change of 11.1°F is equivalent to an epoxy strain of 1%. The optics were bonded at the EKC at an average temperature of 69.83°F , whereas

the temperatures during the ring focus measurements were $69.79\pm 0.05^\circ\text{F}$. This small temperature change is negligible (equivalent to an epoxy strain of 0.0036%).

The finite source distance in the model is 527.27904 meters from the CAP datum A plane. The geometries of the HRMA apertures and their supporting struts are well defined.

The mirror reflectivity was calculated using the optical constants tabulated by Henke et al. (Henke et al., 1993) (0.1–2 keV) and synchrotron measurements made by Graessle et al. (Graessle et al., 1997) (2–12 keV). The mirror surface roughness data from the HDOS WYKO measurements were processed using a program "foldw1", written by L.P. Van Speybroeck, to calculate scattering distributions. The calculation was based on the scattering theory by Beckmann and Spizzichino (Beckmann and Spizzichino, 1963).

The HSI and HRC detectors have spatial resolutions (FWHM) of $14\mu\text{m}$ and $20\mu\text{m}$, respectively. Both detectors have read out pixel size of $6.43\mu\text{m}$.

Of all the elements mentioned above, the 1-g deformation and the epoxy strain are the two central issues for the modeling. While the gravity is constant during the ground tests, epoxy strain can change. That is why we made several measurements during the calibration to determine the epoxy strain change. However, the gravity effect is very strong and the epoxy strain only exhibit very small effect on the ring focus RMS width where the gravity effect dominates.

Figure 18.20 shows the model of ring 1 with Al-K source and all the model elements except the gravity and the epoxy strain effects. The ring width RMS is about 0.5 arcsec with a random noise of the order of 0.1 arcsec. This "noisy" ring width is due to the actual mirror surface imperfection as measured at the HDOS. (For an ideal mirror, the ring width RMS should be 0.01 arcsec with no noise.) As seen from its Fourier transform, there is no noticeable modulations to the general "noisy" shape (the largest term is only 0.015 arcsec. This indicates that there is no significant "structure" in the mirror.

Figure 18.21 shows the model of ring 1 with the 1-g effect but still without the epoxy strain effect. The ring width RMS displays significant split peaks at 30° multiples, except at the top and bottom of the ring. This is the gravity twisting effect at the optic holding points as expected. Notice the base line of this curve is still at about 0.5 arcsec which is set by the mirror surface figure (imperfection). The Fourier transform of the data shows dominant 12 fold symmetry and the second harmonics due to the 12 split peaks, and 2 fold symmetry due to the fact that the peaks are much larger at the sides than at the top and bottom.

Figure 18.22 shows the model of ring 1 with epoxy strain effects in addition to 1-g effects. The top panel shows the mirror with (-2%) TTT initial epoxy cure plus the long term epoxy strains for 1% (fully moist condition) to -1% (fully dried condition). The solid line is the 0.0% moist, i.e. no long term epoxy strain beyond the initial -2% TTT cure strain. When the moisture increases, the epoxy strain would enforce an outward bump at each supporting point. This bump would increase the outward dimple below each supporting point due to the gravity twist, and decrease the inward dimple above each supporting point due to the gravity twist. When the moisture decreases, the epoxy strain would enforce an inward bump at each supporting point, and the effect is reversed. This epoxy strain effect is shown clearly in the Figure 18.22: When the moisture increases (0.5% and 1.0% moist), the peaks 5° outside the 30° multiples (below the supporting points) increase while the peaks 5° inside the 30° multiples (above the supporting points) decrease. When moisture decreases (-0.5% and -1.0% moist), the inside peaks increase while the outside peaks decrease.

As we can see, the effect of epoxy strain change is very dramatic at this 1% level. The actual data (Figures 18.15–18.18) show little noticeable effect like this. Therefore we conclude that the epoxy strain change must be significantly less than 1%.

18.6 Comparison of Data with the Model

To see if there were any changes in the ring structure, we compare the ring focus data taken on 1996/12/23, 1997/02/10 and 1997/04/10. The first two images were taken with the HSI at the beginning and the end of the phase 1 calibration, separated by 1.5 months. The third image was taken with the HRC two months later, in the phase 2 calibration. Figures 18.23–18.26 show the comparison. As in Figures 18.15–18.18, the top panels show the ring width RMS variations and the bottom panels show their Fourier transforms. As it can be seen, there are indeed changes in the ring structure during the calibration period. Generally, there were relatively larger change between 1996/12/23 and 1997/02/10, and relatively smaller change between 1997/02/10 and 1997/04/10.

For a closer look, Figures 18.27–18.30 show the ring width RMS change from 1996/12/23 to 1997/02/10. They were both taken with the Al-K source. The top panels show the two RMS curves. For most of the double peaks, especially on the left (north), the inside peaks increased while the outside peaks decreased. According to the analysis in the previous section, this indicates the possibility of inward bump at the flexures due to the moisture decrease in the epoxy. However, this change is not very consistent. On the right side of ring 1, there is very little change. Peaks at 150° from all four rings and some peaks on the right side of ring 3 seem have the opposite change (i.e. inside peaks decreased while outside peaks increased). The second panels show the Fourier transforms of the above two curves. The third panels show the differences of the two RMS curves (RMS of 1997/02/10 minus RMS of 1996/12/23). The bottom panels show the Fourier transform of the difference. In general, the changes in the RMS width are very small – at the 0.1 arcsec level.

Figures 18.31–18.34 show the ring width RMS change from 1997/02/10 to 1997/04/10. Generally, the changes were smaller during that two months period comparing to the first month and half (compare the third, RMS difference, panel for each ring). This indicates the HRMA is likely stabilized from epoxy strain distortion after the first month and half in the calibration chamber.

The small change in the ring width could be due to the temperature, gravity or the epoxy strain. The temperature during the measurements, as mentioned earlier, was very constant and very close to the temperature as the HRMA was assembled. Therefore the temperature effect is negligible. Gravity could have caused small changes if the HRMA support conditions were changed during that period. This is possible as the test vacuum chamber was opened a few times and work was done on the HRMA actuators. However, we do not have enough convincing data and information to model this scenario. Supposing the change was purely due to the epoxy strain, which is the most likely case, we can give an estimate of the change based on our model.

Figure 18.35 shows the model for ring 1 with the epoxy strain of -2% TTT plus 0.0% and -0.3% moist. The four panels show the same curves as shown in Figure 18.27 with the same scale. As mentioned above, most of the epoxy strain changes seem occurred in phase 1, i.e. between 1996/12/23 and 1997/02/10. We compare Figure 18.35 with Figure 18.27, and see many similarities and also differences:

1. The width RMS curves (top panels) of both data and model have the same base line of about 0.5 arcsec. This indicates that the model for the mirror surface figure is correct.
2. Both curves (top panels) have 12 dominant split peaks at 30° multiples. Both of their Fourier transforms (second panels) have dominant 2, 12 and 24 fold symmetries and about the same magnitude of 12 ± 1 , ± 2 and 24 ± 1 , ± 2 components. This indicates that the 1-g model is right.
3. The model has larger modulation amplitude than that of the data (top and second panels). This indicates that the epoxy strain change is likely less than 0.3%.

4. The model show the inside peaks increase and outside peaks decrease on both sides of the curve (top panels) due to the epoxy moisture loss, while the data only shows this effect on the left side (-180° to 0°). This could be due to the HRMA loading condition changed during the test. It could also be due to the epoxy moisture condition was not uniform to begin with.
5. The RMS difference curves show similar structures between the data and the model. Only the data has smaller amplitude on the right side (0° to 180°); this agrees with the discussion in the previous paragraph.

18.7 Conclusion

The HRMA ring focus measurements were made with the HSI and HRC detectors during the HRMA calibration. From 1996/12/23 to 1997/04/10, five HSI images and one HRC image were taken. The data show the RMS ring width has 12 dominate split peaks around the center line of the 12 mirror holding flexures. The ring focus model was generated using raytracing, considering all the relevant factors from the mirror surface figure to the XRCF test environment. By comparing the ring focus data and the ring focus models, we are able to assess the mirror surface figures as well as the mechanical support system distortions which are very difficult to detect in the focal plane. We also estimated the epoxy strain effects on the mirror for its on-orbit performance.

These are the conclusions of this study:

1. In general, the model and the data agree well. Effects of mirror surface figure, assembly errors, decenter and tilt, finite source distance, gravity etc. are clearly shown in the model and agree with the data.
2. Inside peaks increased and outside peaks decreased during the first month and half of the calibration. This is consistent with the theoretical model of epoxy strain due to moisture loss.
3. Comparing the data with the model, the actual change in the epoxy strain is very small ($\sim 0.3\%$). The small epoxy strain change could be because most of the moisture loss in the epoxy bond occurred before the beginning of ring focus measurements, due to the HRMA vacuum exposure and dry nitrogen purge used after the final assembly.
4. Changes between 2/10 and 4/10 are even smaller than the changes occurred between 12/23/96 and 2/10/97. This indicates the HRMA has likely stabilized from epoxy strain distortion after the first month and half in the calibration chamber.
5. The small change of the epoxy strain and its stabilization observed during the calibration interval lead us to expect no more serious changes between the calibration and flight performance. Even in a worst case, it is unlikely the epoxy strain effect on-orbit will be more than 0.5% due to moisture loss. A raytrace calculation with the 1-g effect removed shows that this case will degrade the AXAF performance by no more than 5% from a one arc second diameter encircled energy for mirror pair 1. The change of the epoxy strain on other shells is even less than that measured on shell 1, and hence the total effect should be less than 5% loss for the whole HRMA.
6. We should be able to predict the HRMA on-orbit performance using the ground calibration data.

Here is the bottom line: HRMA IS AN EXCELLENT MIRROR. IT WILL STAY THAT WAY ON ORBIT!

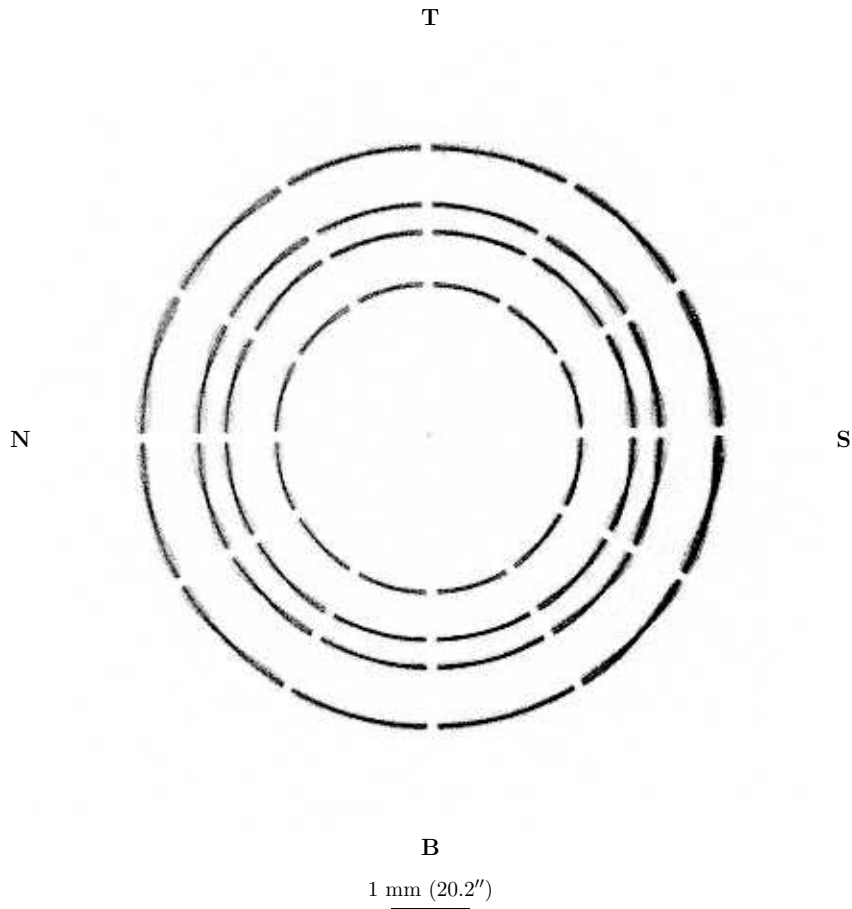


Figure 18.1: The HRMA ring focus HSI image. Date: 1996/12/23; TRW ID: C-IXH-RF-1.005; Run ID: 106856; Source: Al-K; Defocus: 65.2 mm; Integration time: 1800 seconds.

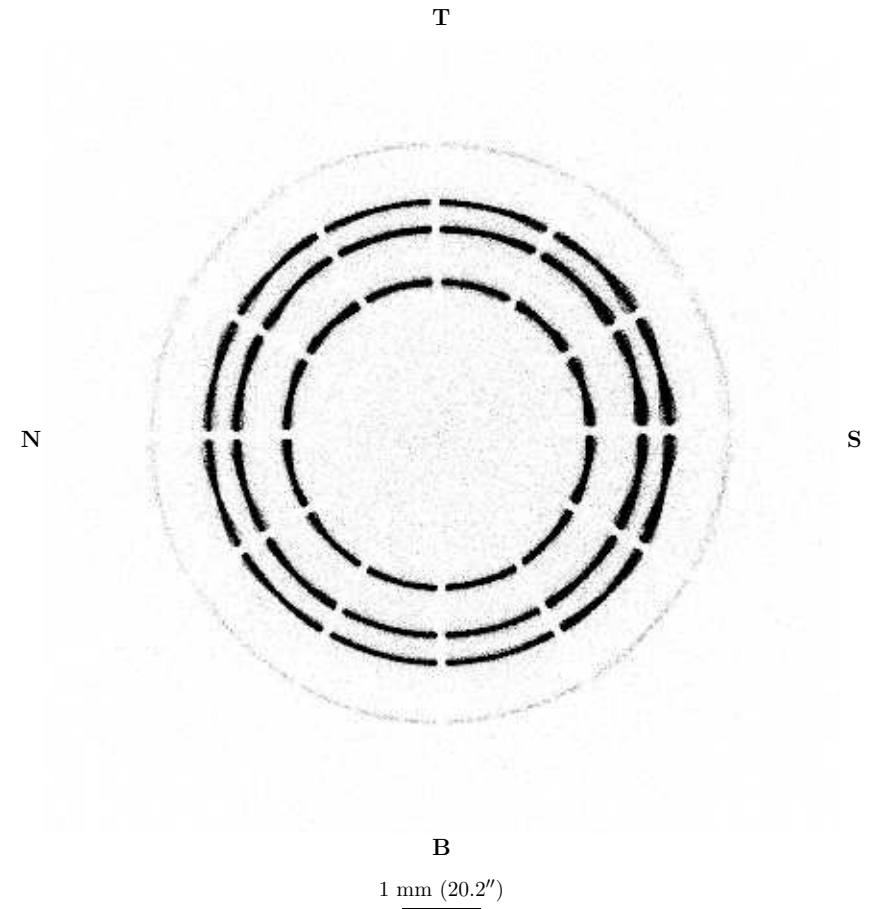


Figure 18.2: The HRMA ring focus HSI image. Date: 1997/01/10; TRW ID: D-IXH-RF-1.003; Run ID: 108185; Source: Fe-K; Defocus: 65.2 mm; Integration time: 1800 seconds.

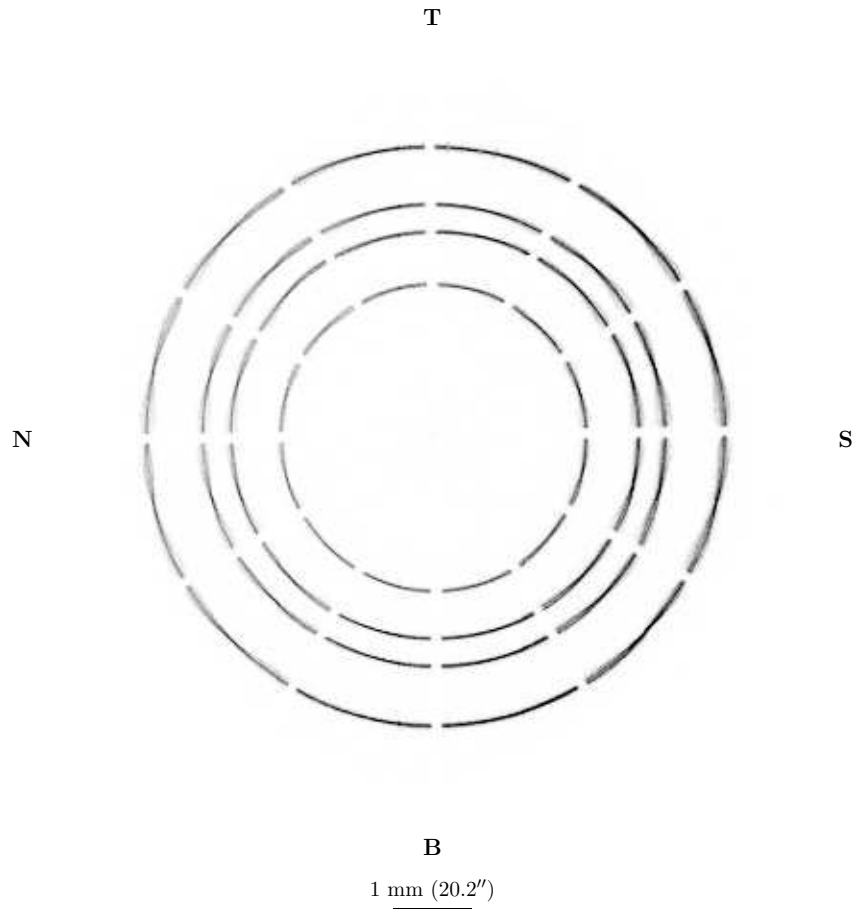


Figure 18.3: The HRMA ring focus HSI image. Date: 1997/01/15; TRW ID: D-IXH-RF-1.002; Run ID: 108944; Source: C-K; Defocus: 65.2 mm; Integration time: 1800 seconds.

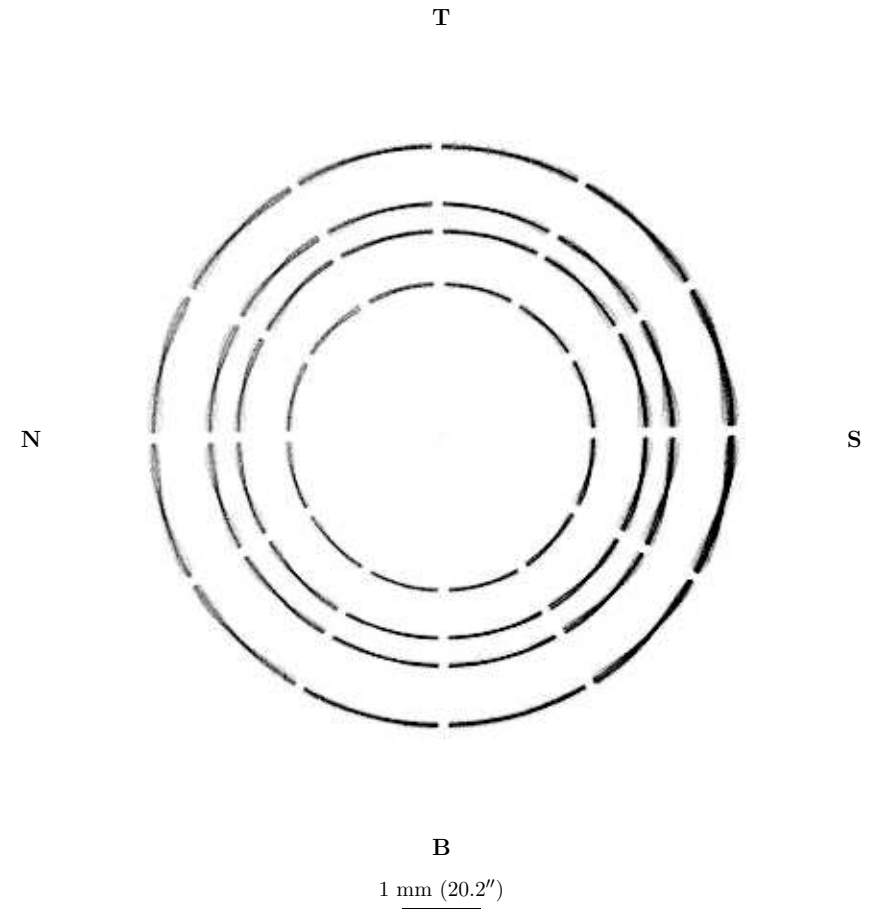


Figure 18.4: The HRMA ring focus HSI image. Date: 1997/01/24; TRW ID: D-IXH-RF-1.005; Run ID: 110004; Source: A1-K; Defocus: 65.2 mm; Integration time: 1800 seconds.

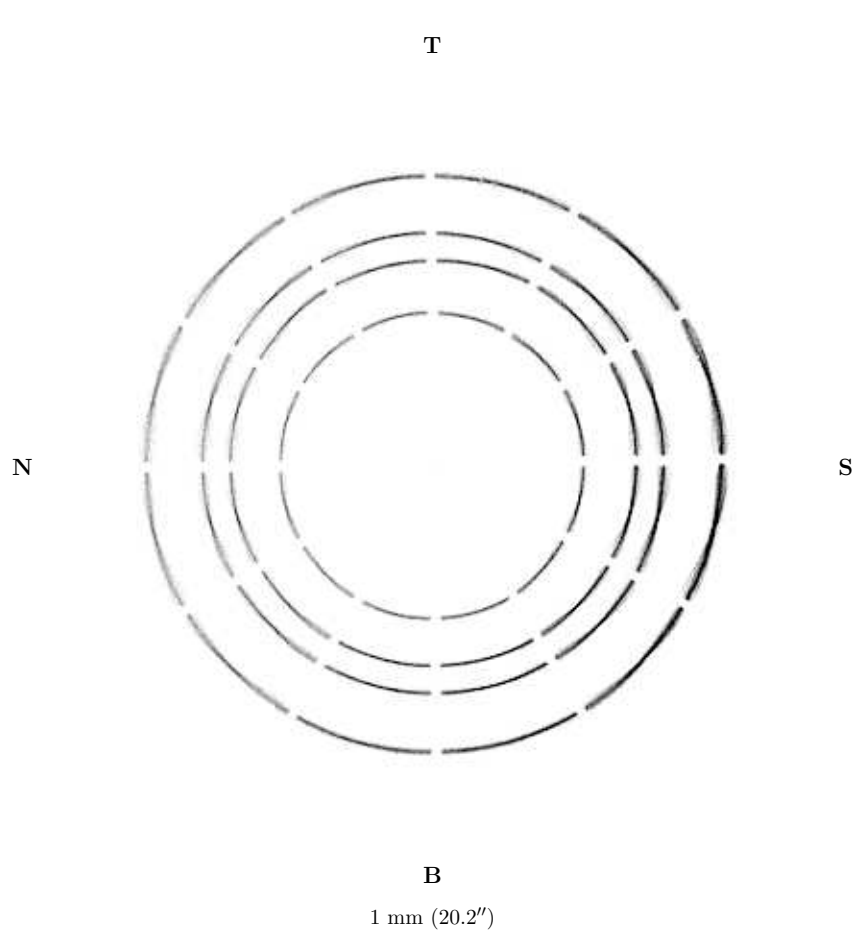


Figure 18.5: The HRMA ring focus HSI image. Date: 1997/02/10; TRW ID: E-IXH-RF-1.007; Run ID: 111804; Source: Al-K; Defocus: 65.2 mm; Integration time: 1800 seconds.

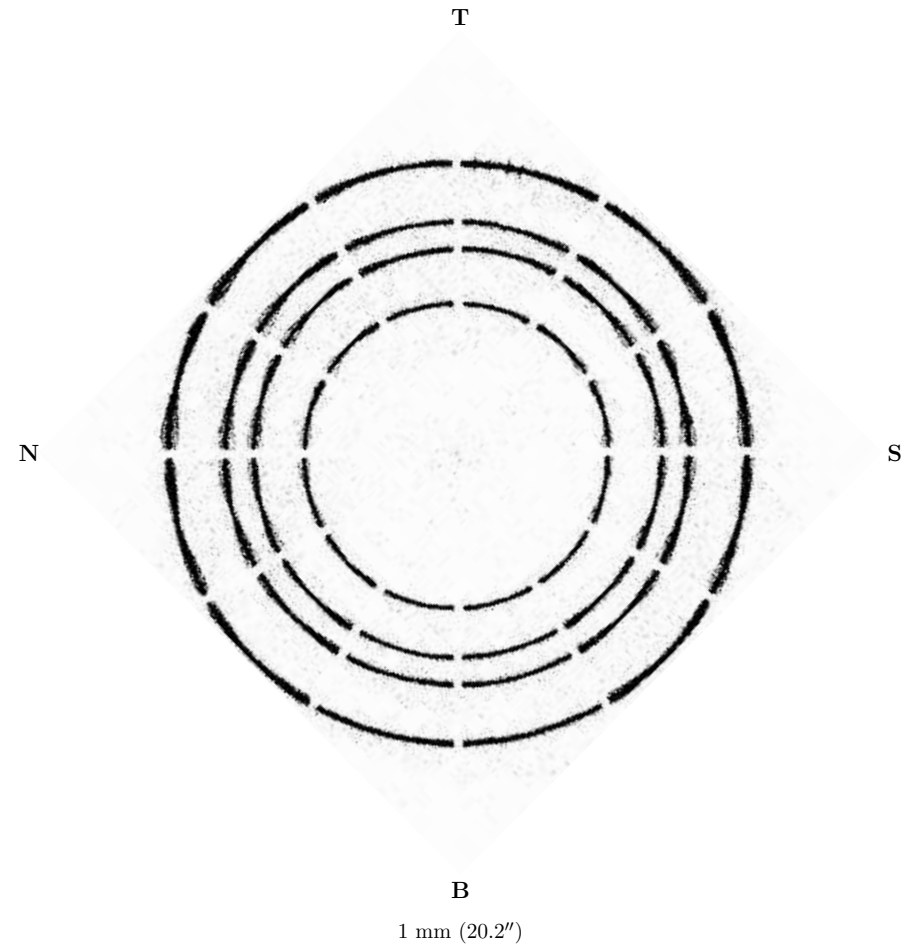


Figure 18.6: The HRMA ring focus HRC image. Date: 1997/04/10; TRW ID: G-IHI-RF-7.007; Run ID: 114828; Source: Mg-K; Defocus: 65.2 mm; Integration time: 6000 seconds.

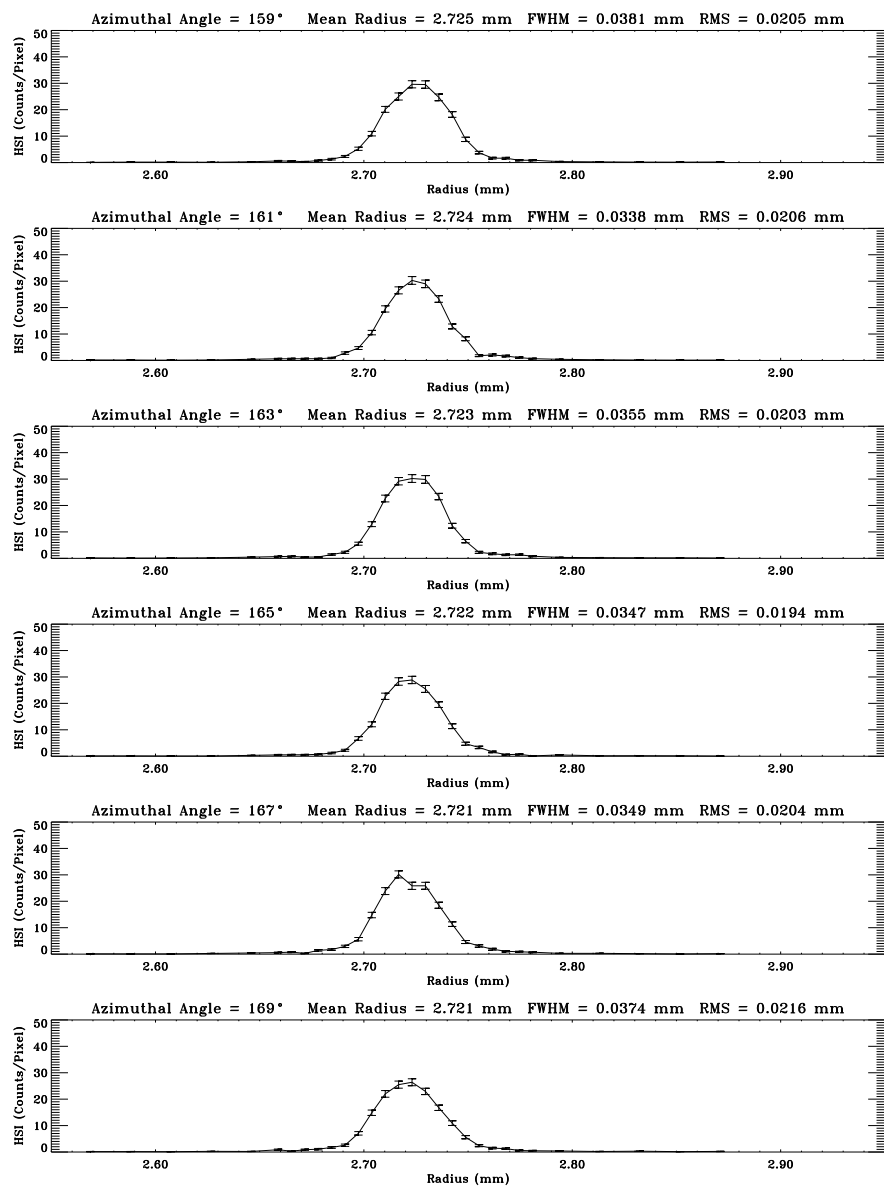


Figure 18.7: Radial profiles for ring 4. Date: 1997/01/24; TRW ID: D-IXH-RF-1.005; Run ID: 110004; Source: Al-K; Defocus: 65.2 mm.

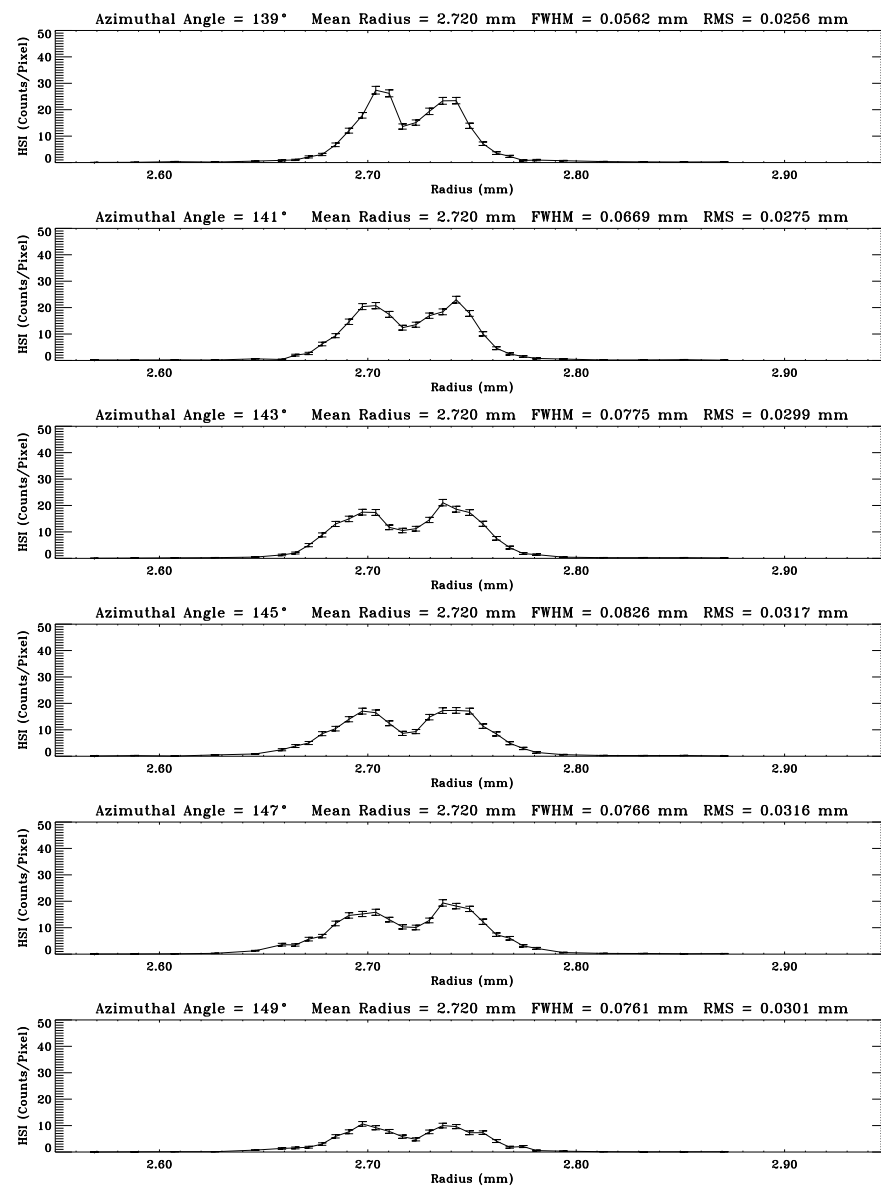


Figure 18.8: Radial profiles for ring 4. Date: 1997/01/24; TRW ID: D-IXH-RF-1.005; Run ID: 110004; Source: Al-K; Defocus: 65.2 mm.

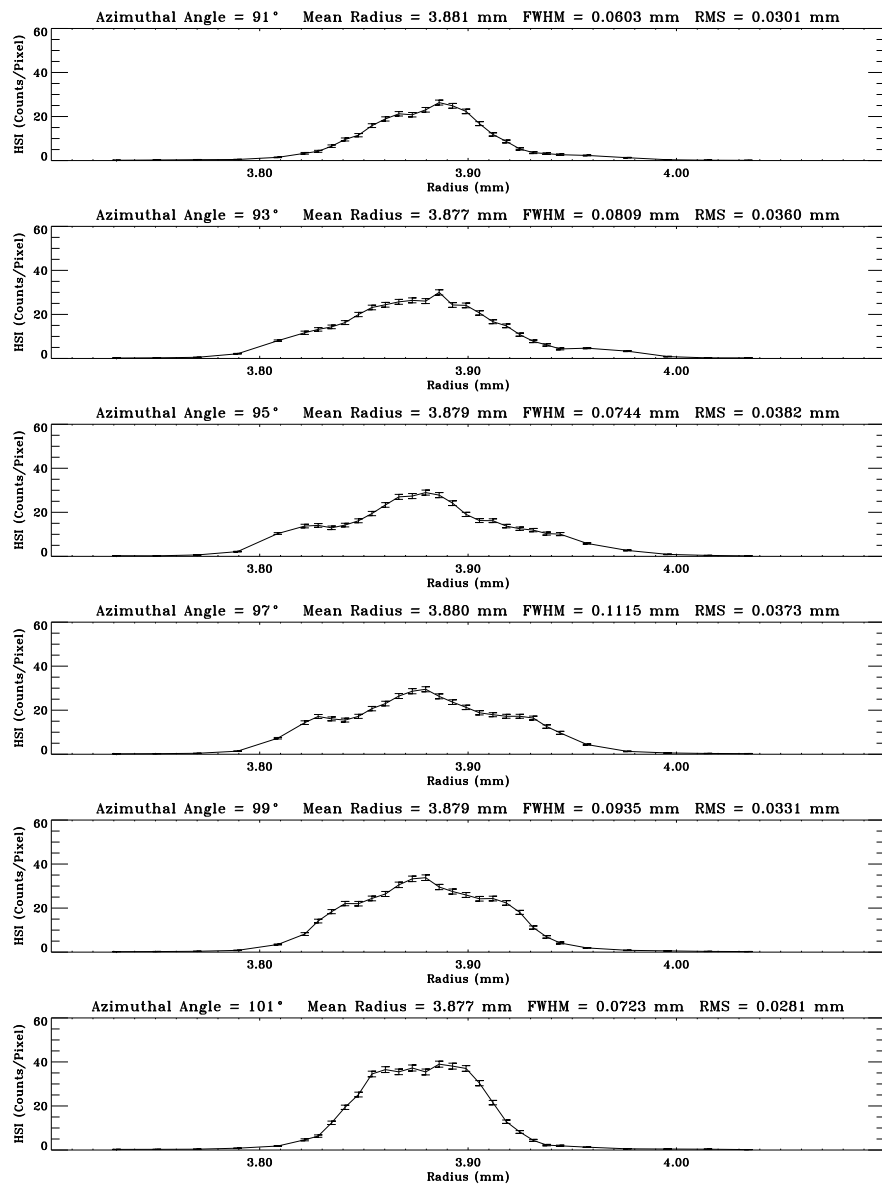


Figure 18.9: Radial profiles for ring 1. Date: 1997/01/24; TRW ID: D-IXH-RF-1.005; Run ID: 110004; Source: Al-K; Defocus: 65.2 mm.

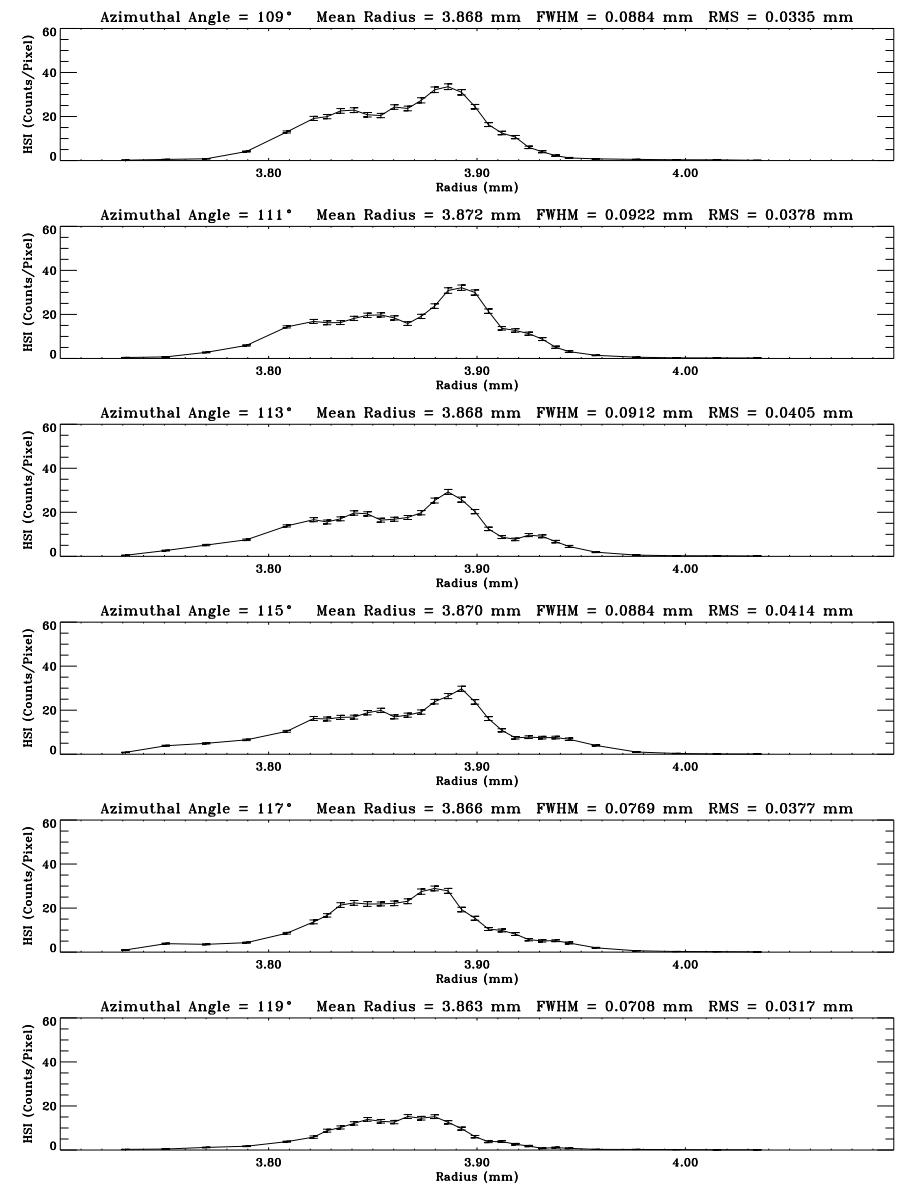


Figure 18.10: Radial profiles for ring 1. Date: 1997/01/24; TRW ID: D-IXH-RF-1.005; Run ID: 110004; Source: Al-K; Defocus: 65.2 mm.

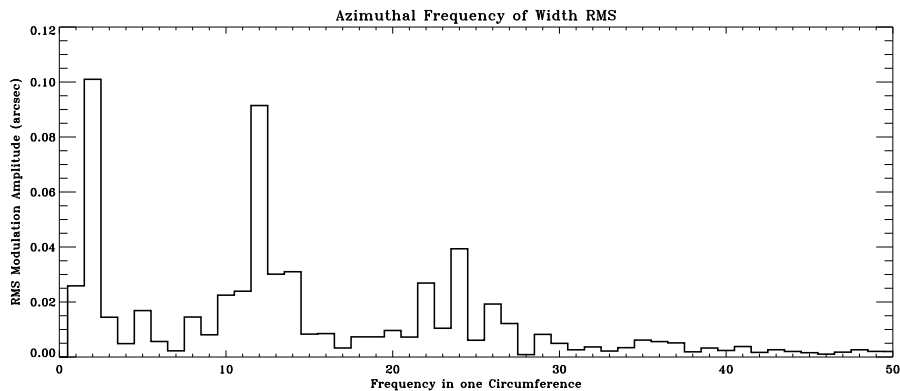
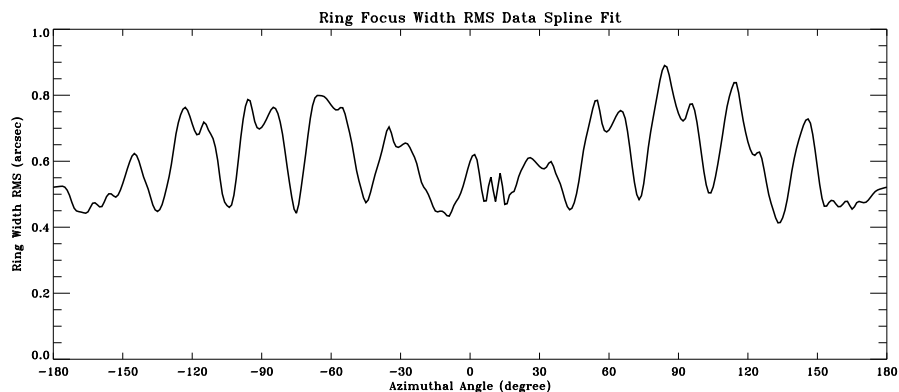
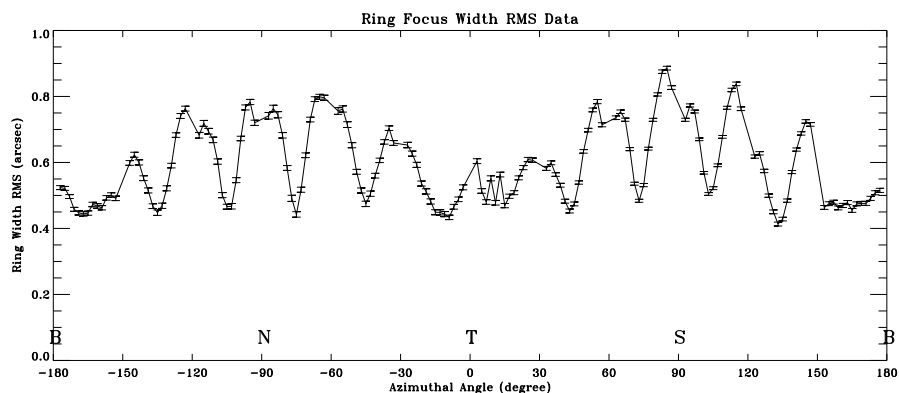


Figure 18.11: The Ring width RMS for ring 1. Date: 1997/01/24; TRW ID: D-IXH-RF-1.005; Run ID: 110004; Source: Al-K; Defocus: 65.2 mm.

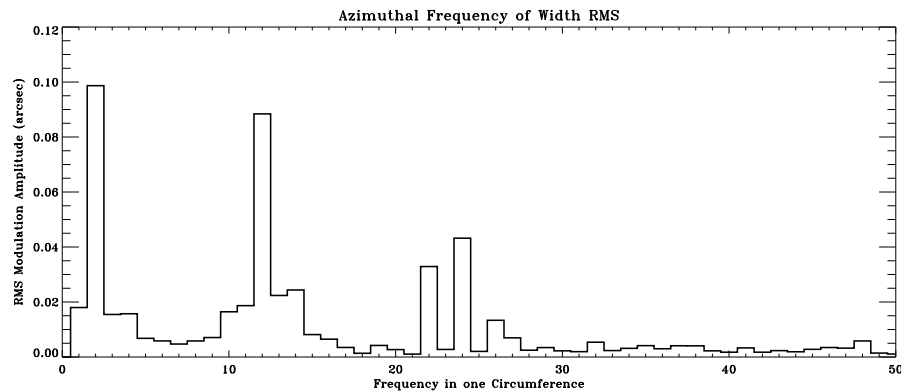
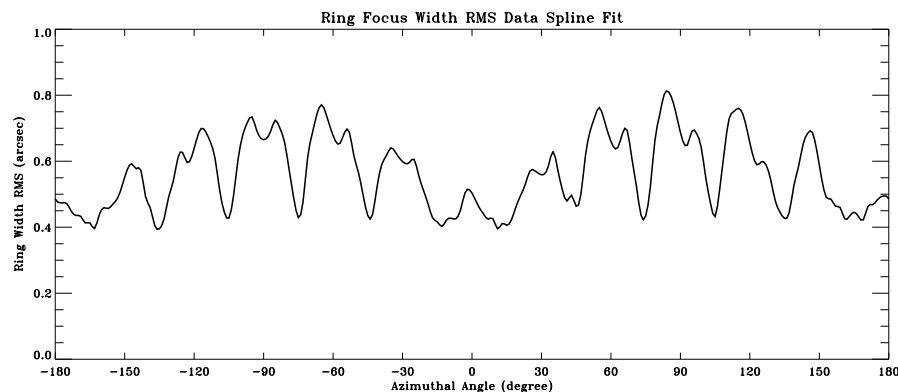
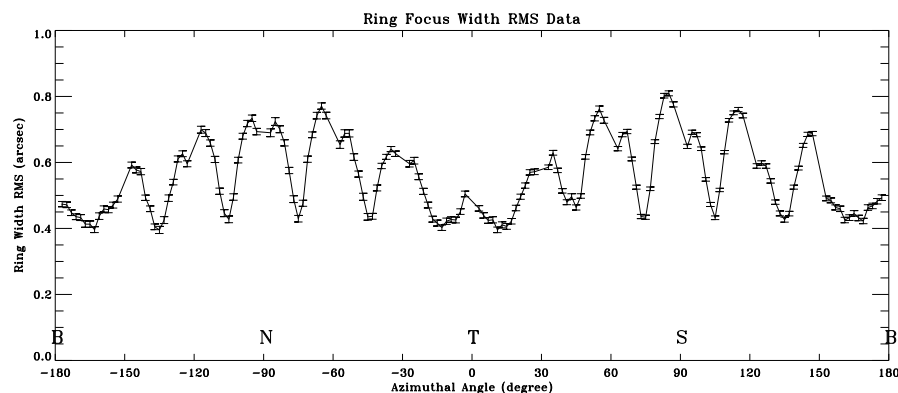


Figure 18.12: The Ring width RMS for ring 3. Date: 1997/01/24; TRW ID: D-IXH-RF-1.005; Run ID: 110004; Source: Al-K; Defocus: 65.2 mm.

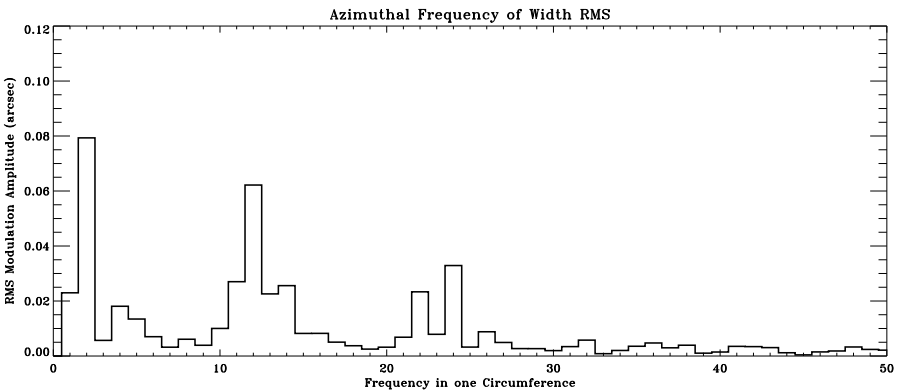
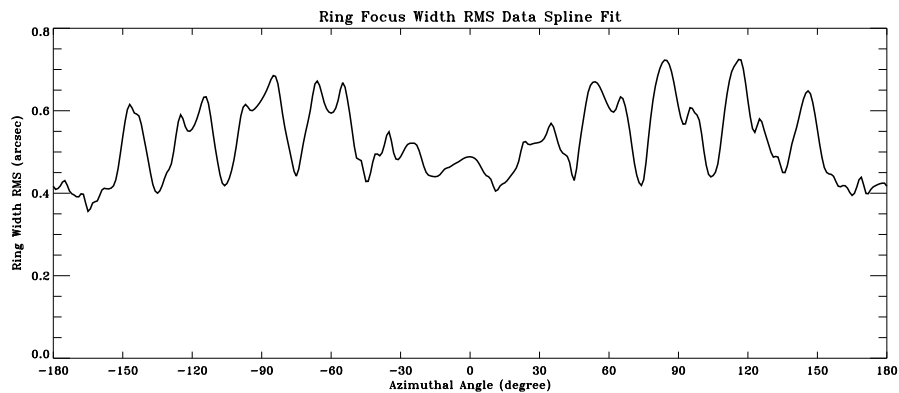
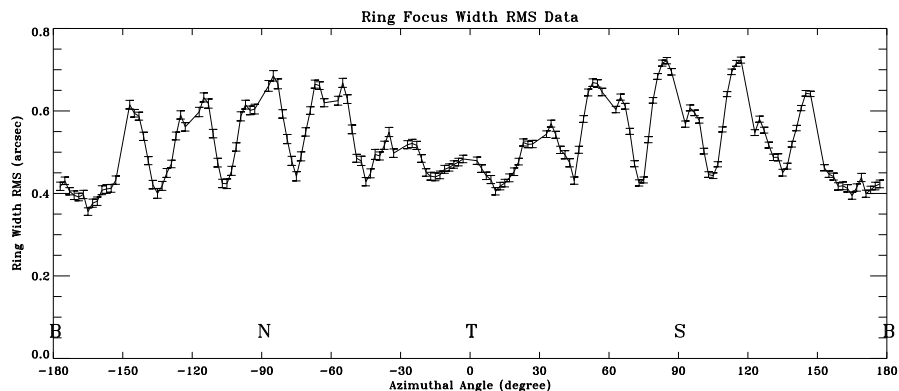


Figure 18.13: The Ring width RMS for ring 4. Date: 1997/01/24; TRW ID: D-IXH-RF-1.005; Run ID: 110004; Source: Al-K; Defocus: 65.2 mm.

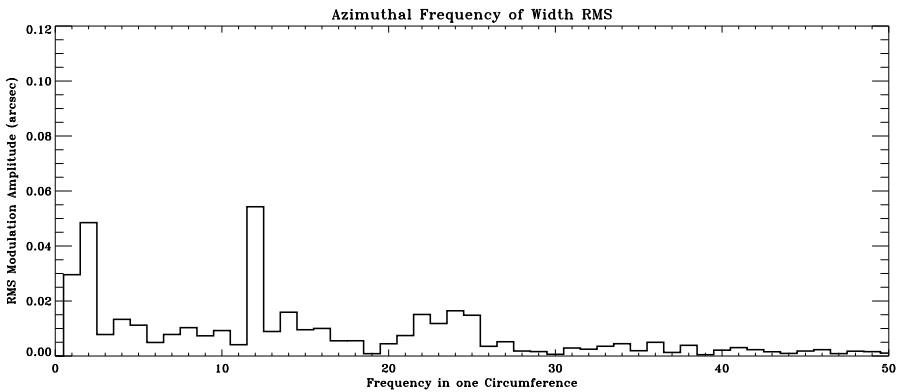
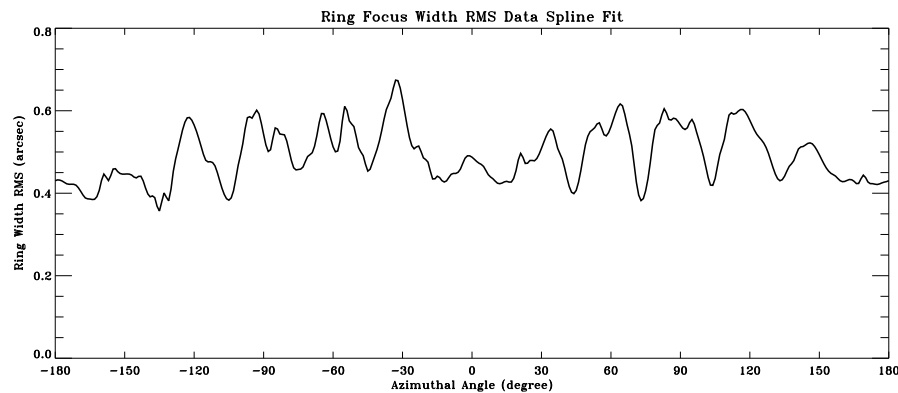
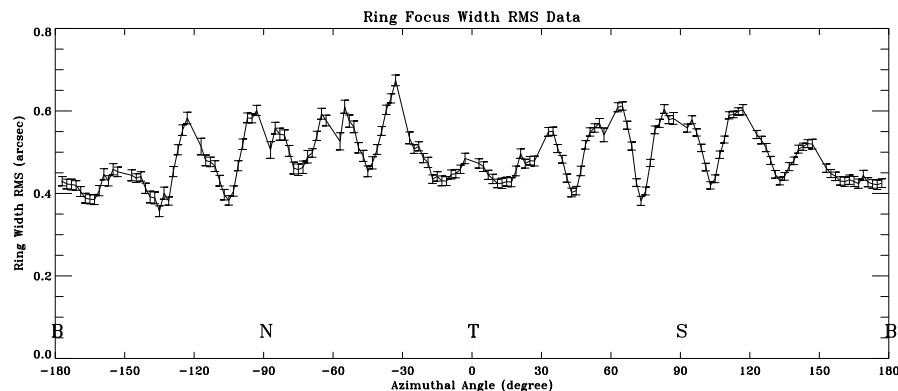


Figure 18.14: The Ring width RMS for ring 6. Date: 1997/01/24; TRW ID: D-IXH-RF-1.005; Run ID: 110004; Source: Al-K; Defocus: 65.2 mm.

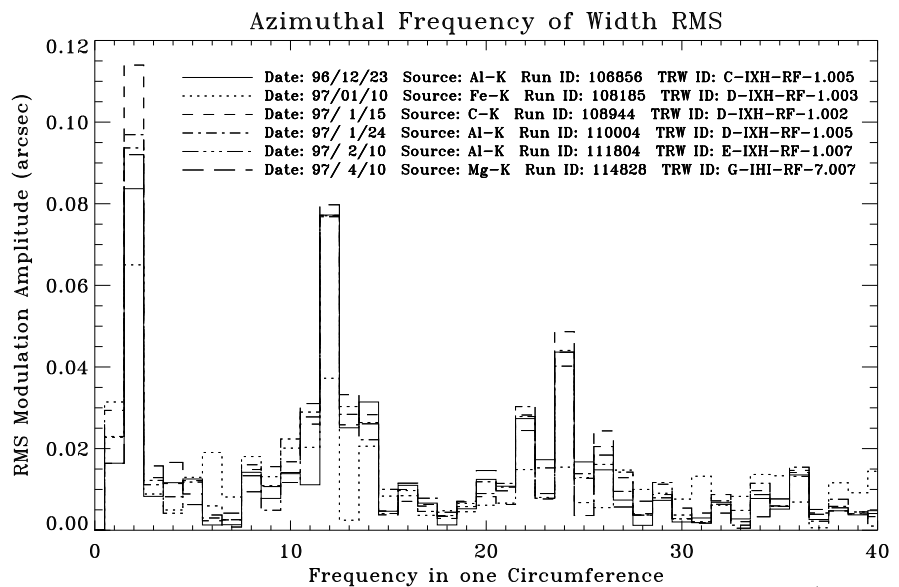
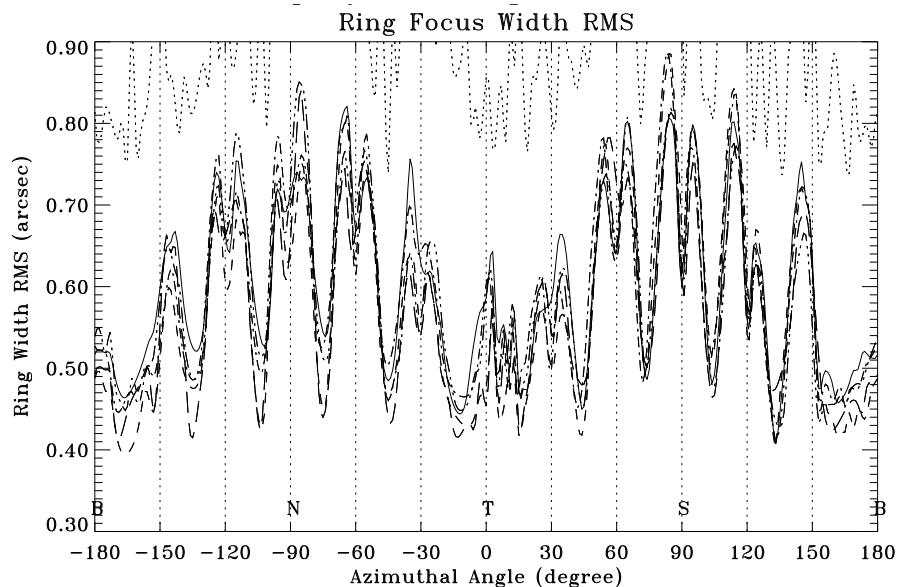


Figure 18.15: The Ring width RMS for ring 1, from all six ring focus measurements.

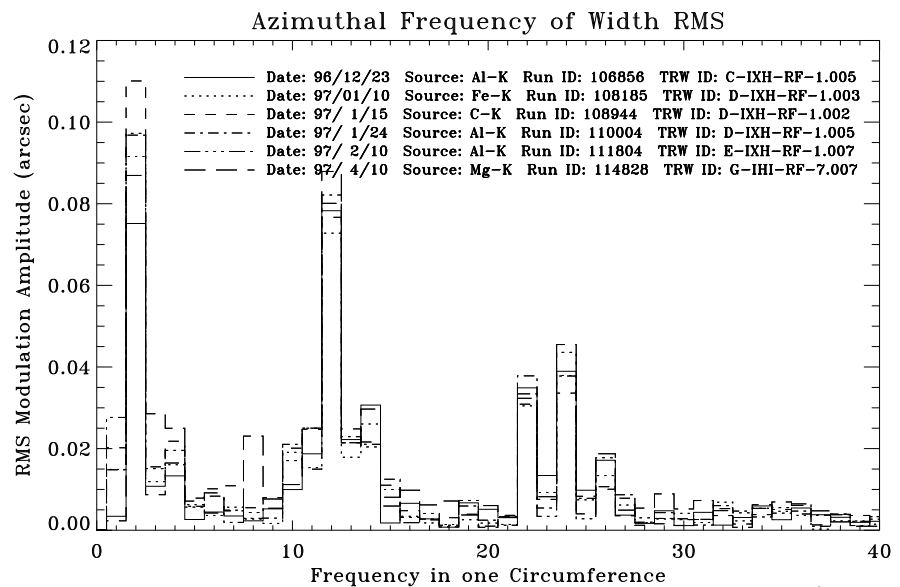
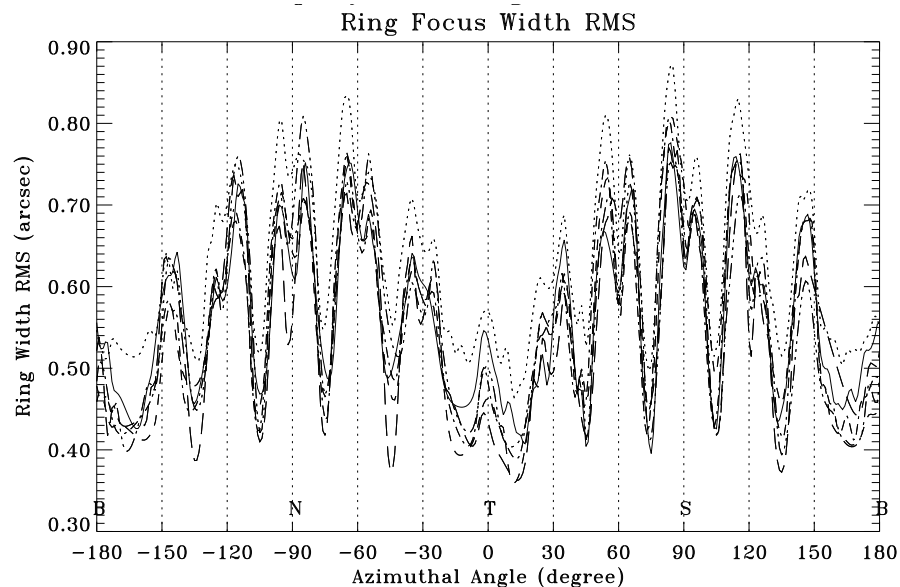


Figure 18.16: The Ring width RMS for ring 3, from all six ring focus measurements.

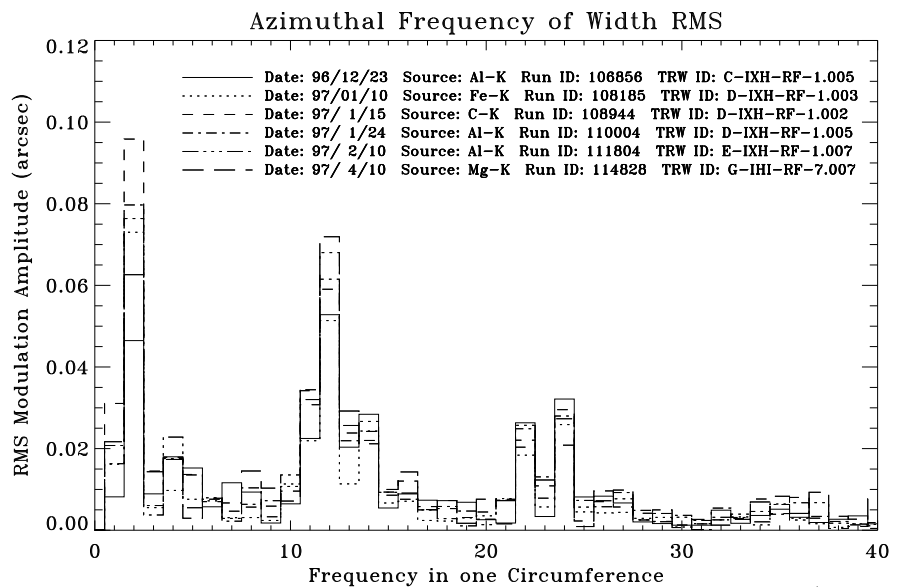
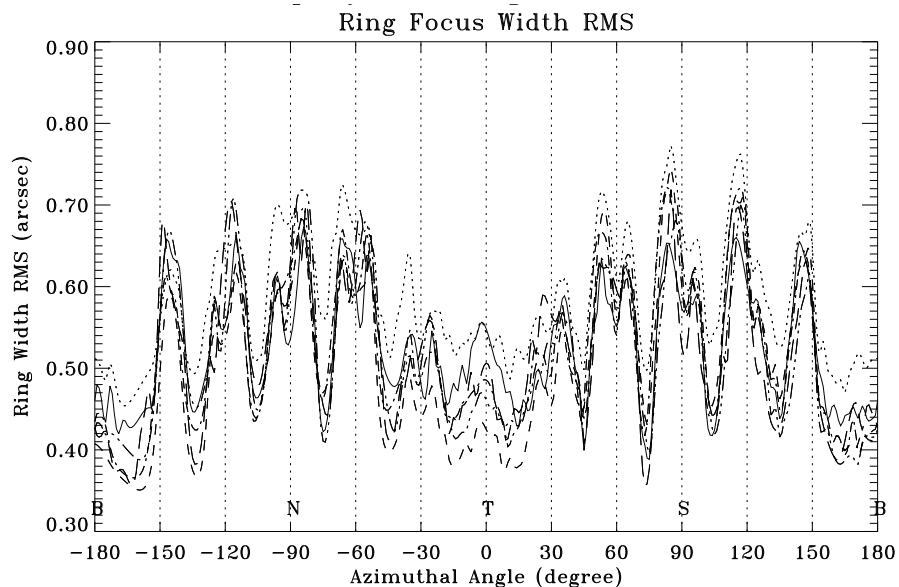


Figure 18.17: The Ring width RMS for ring 4, from all six ring focus measurements.

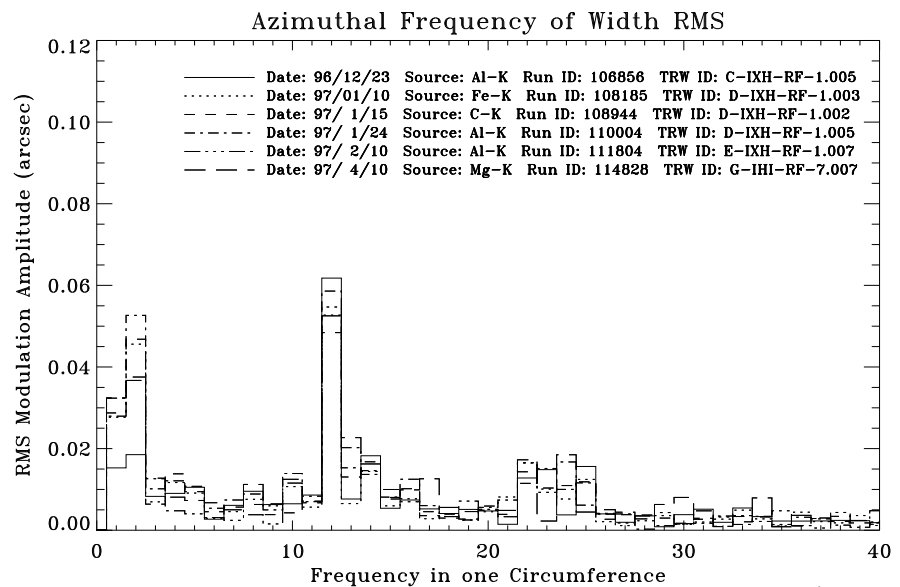
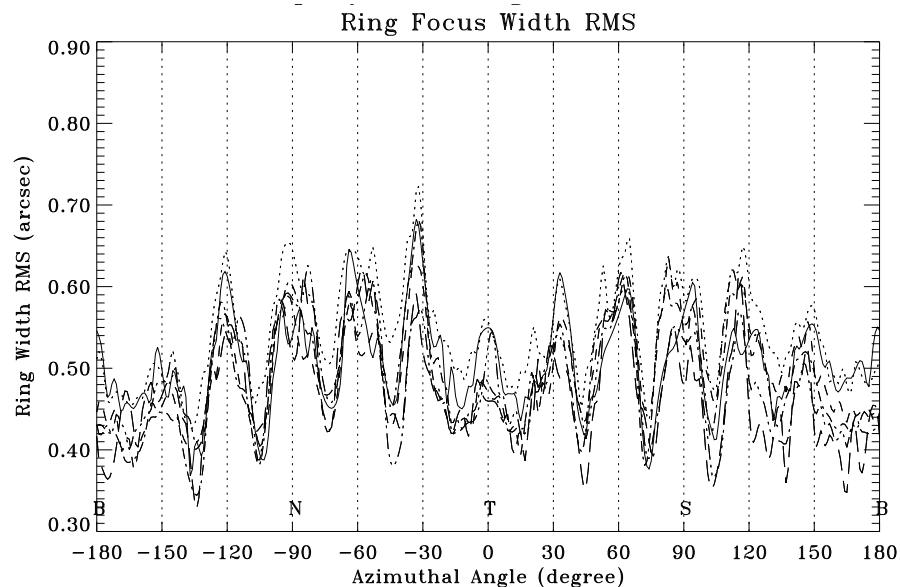


Figure 18.18: The Ring width RMS for ring 6, from all six ring focus measurements.

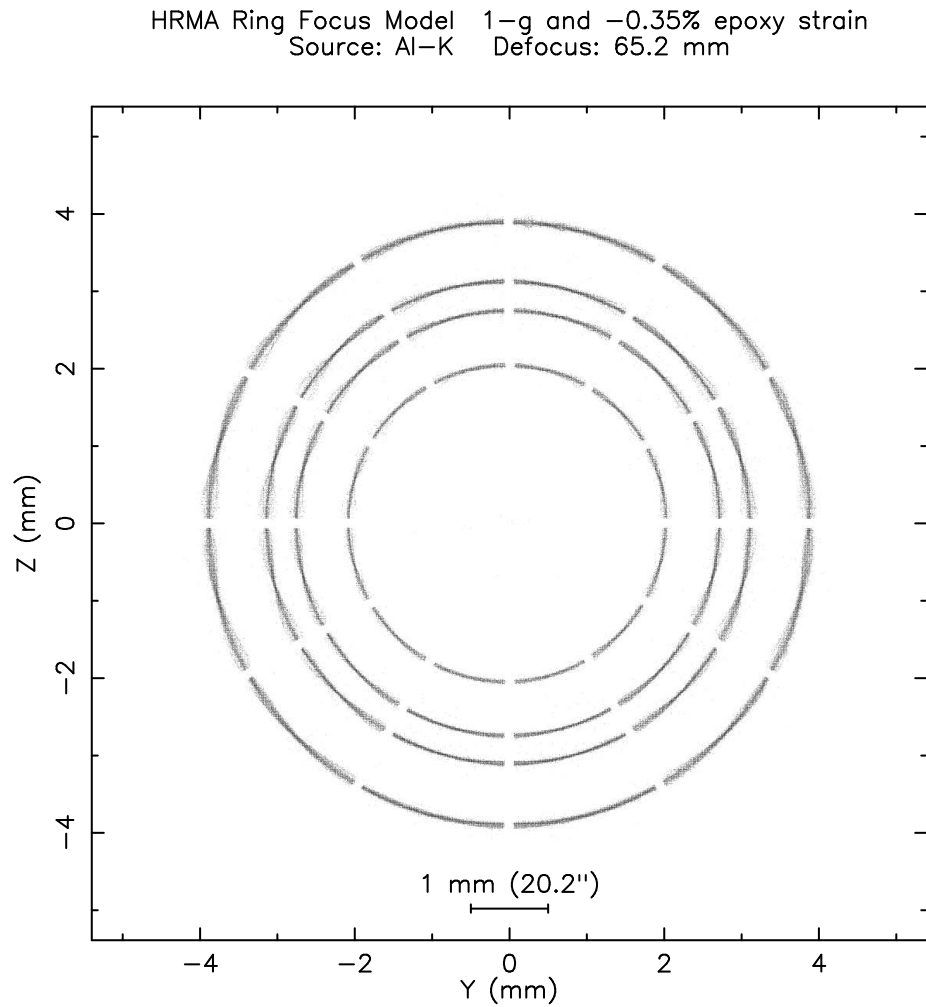


Figure 18.19: The HRMA ring focus model with -0.5% epoxy strain. Source: Al-K; Defocus: 65.2 mm

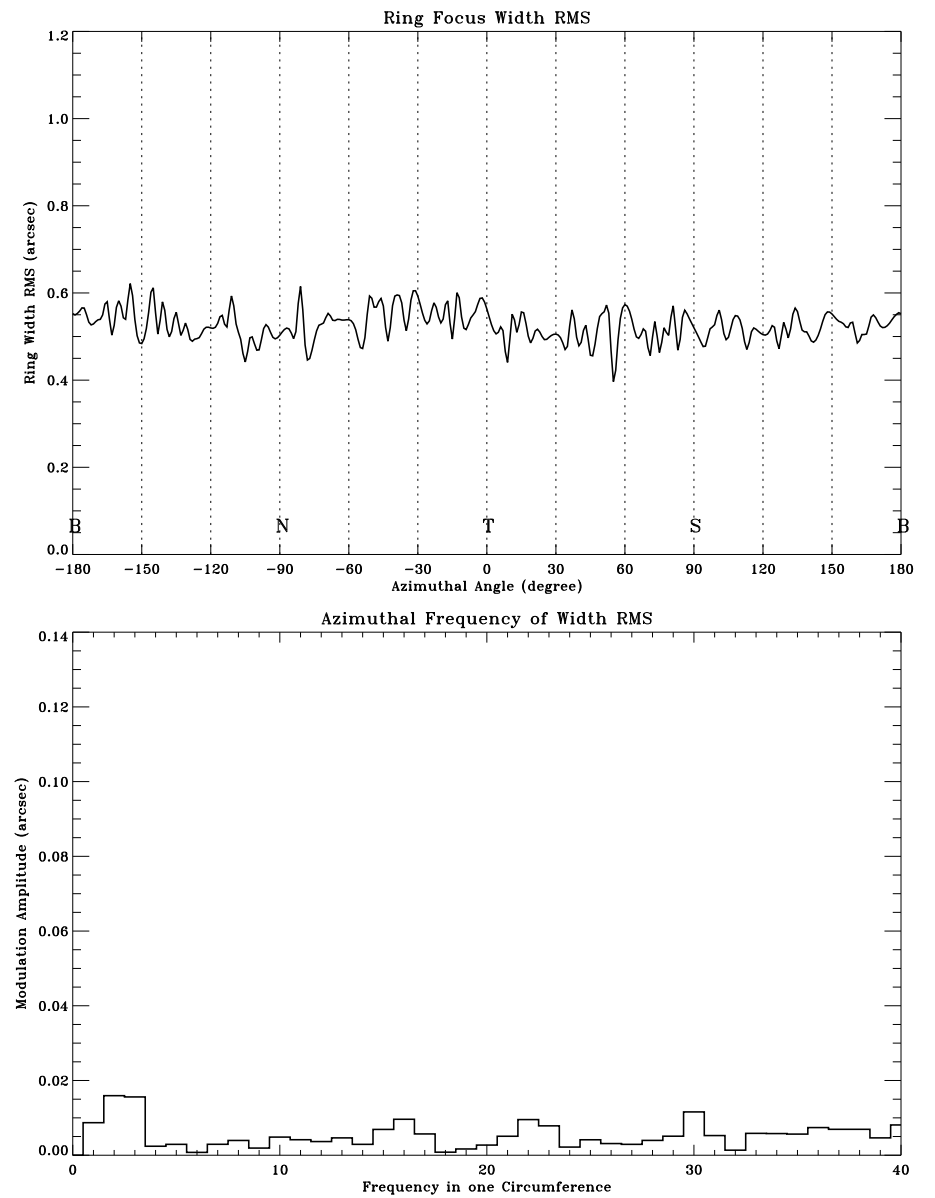


Figure 18.20: HRMA ring focus model: Ring 1, Al-K source, no gravity, no epoxy strain.

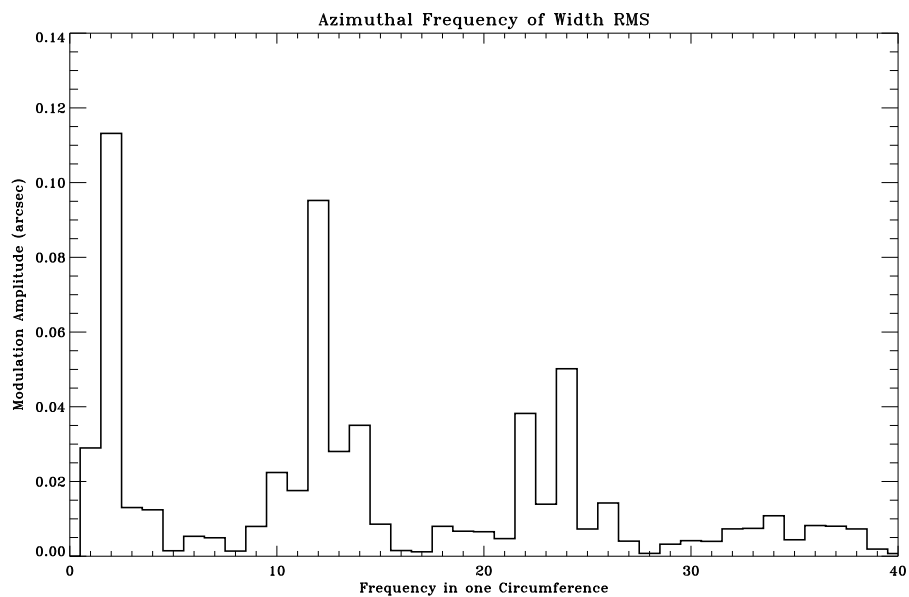
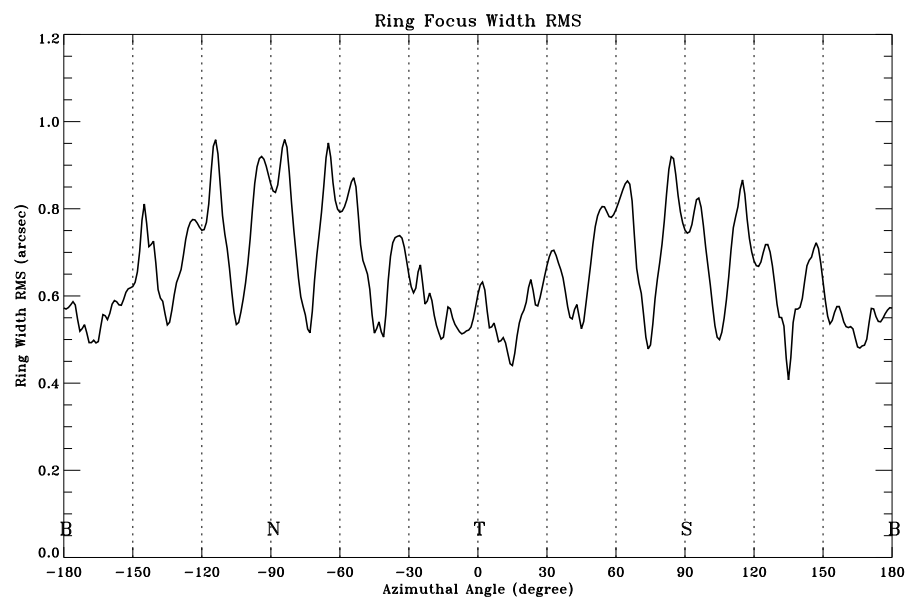


Figure 18.21: HRMA ring focus model: Ring 1, Al-K source, with gravity, no epoxy strain.

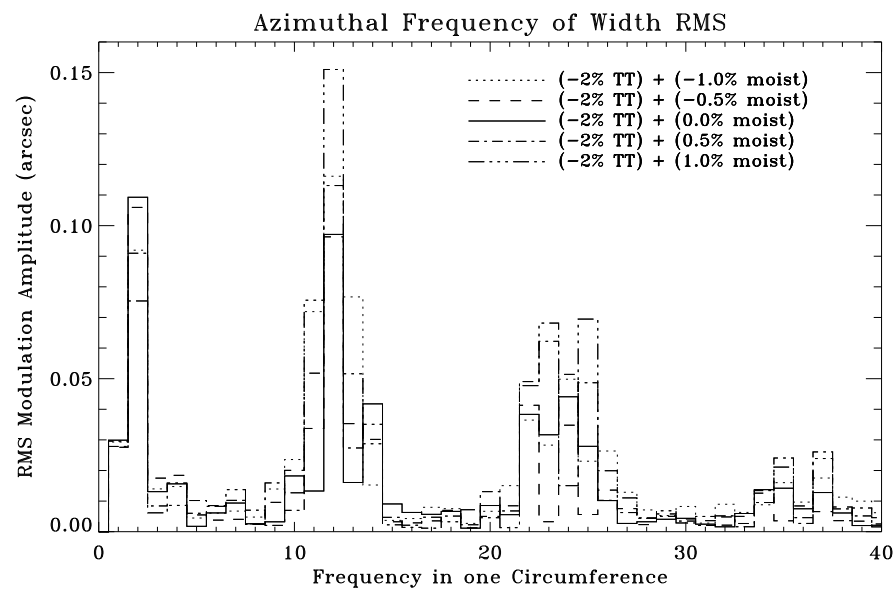
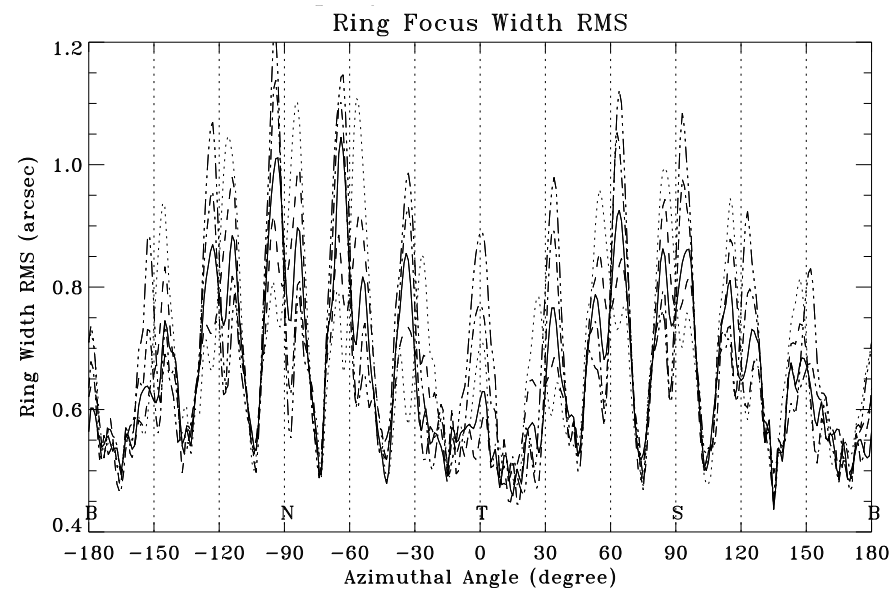


Figure 18.22: HRMA ring focus model: Ring 1, Al-K source, with gravity and epoxy strain change.

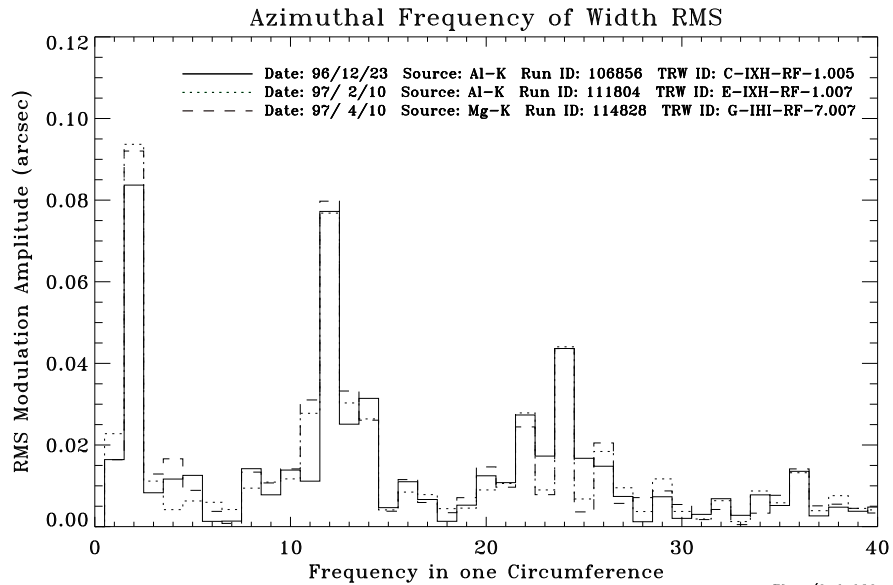
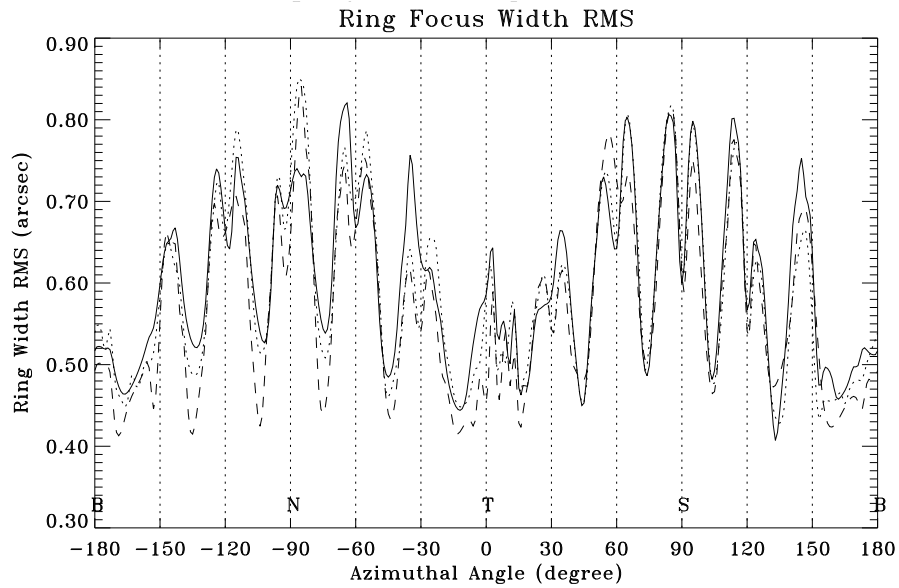


Figure 18.23: The Ring width RMS for ring 1, from three ring focus measurements on 1996/12/23, 1997/02/10 and 1997/04/10.

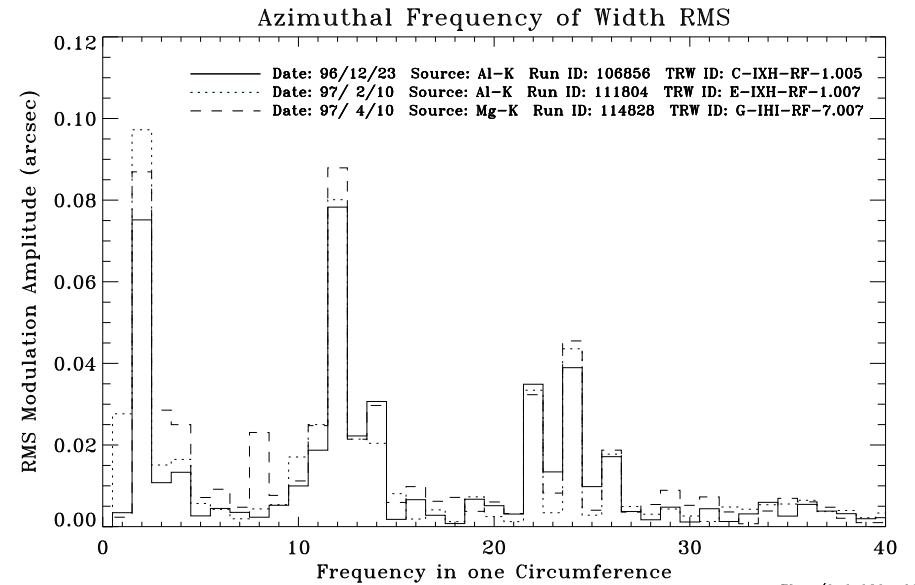
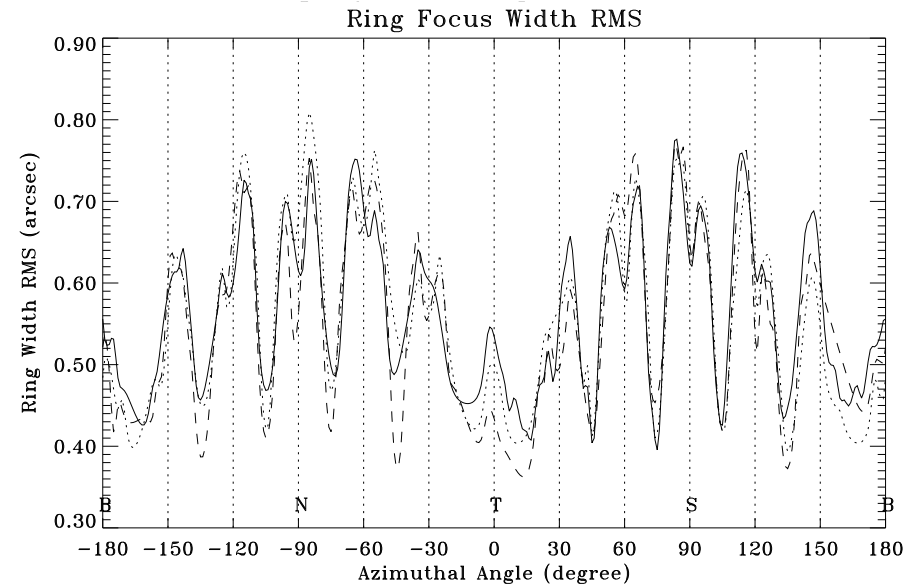


Figure 18.24: The Ring width RMS for ring 3, from three ring focus measurements on 1996/12/23, 1997/02/10 and 1997/04/10.

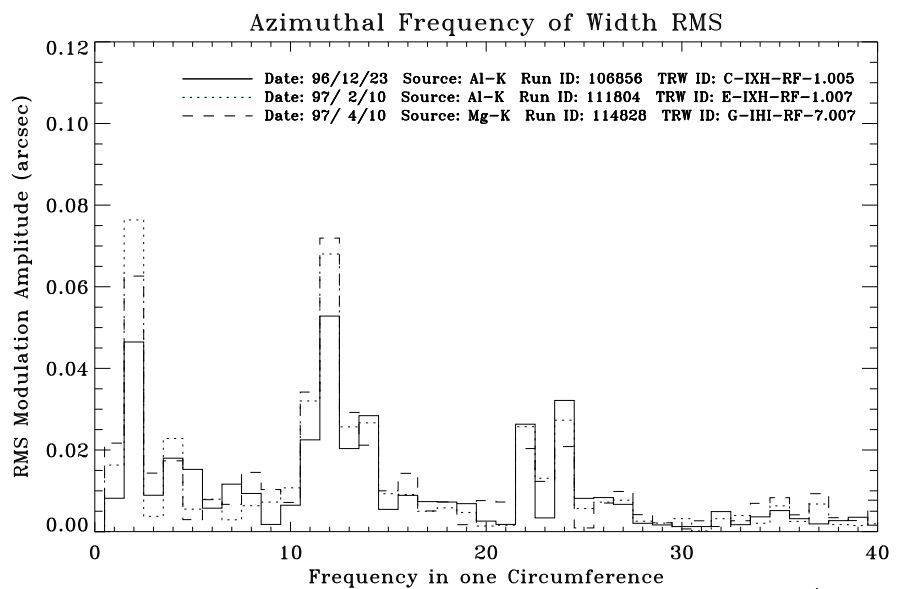
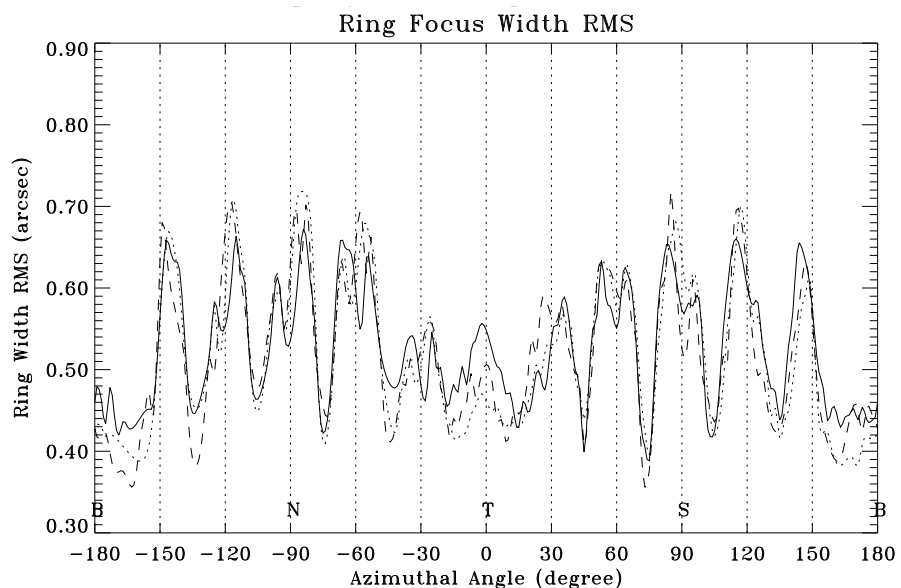


Figure 18.25: The Ring width RMS for ring 4, from three ring focus measurements on 1996/12/23, 1997/02/10 and 1997/04/10.

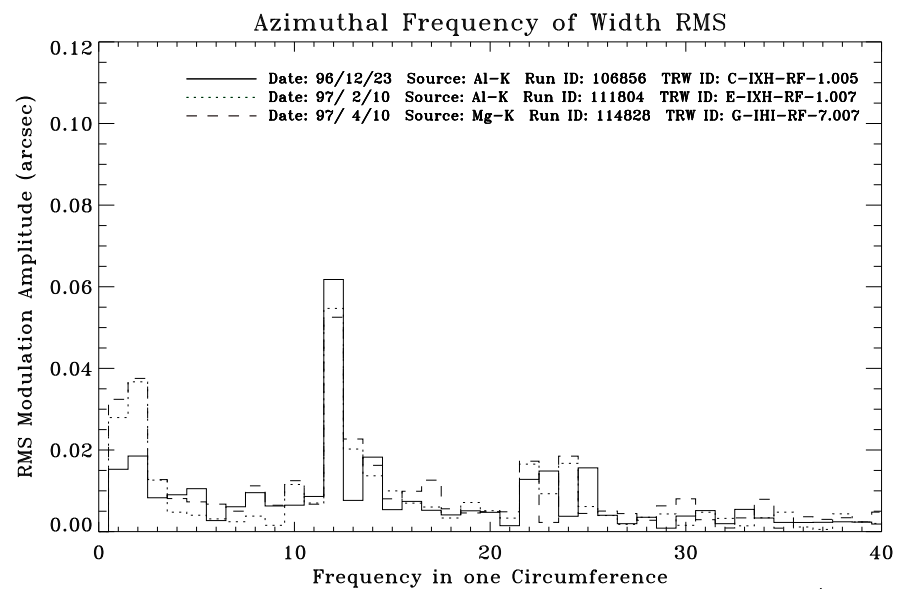
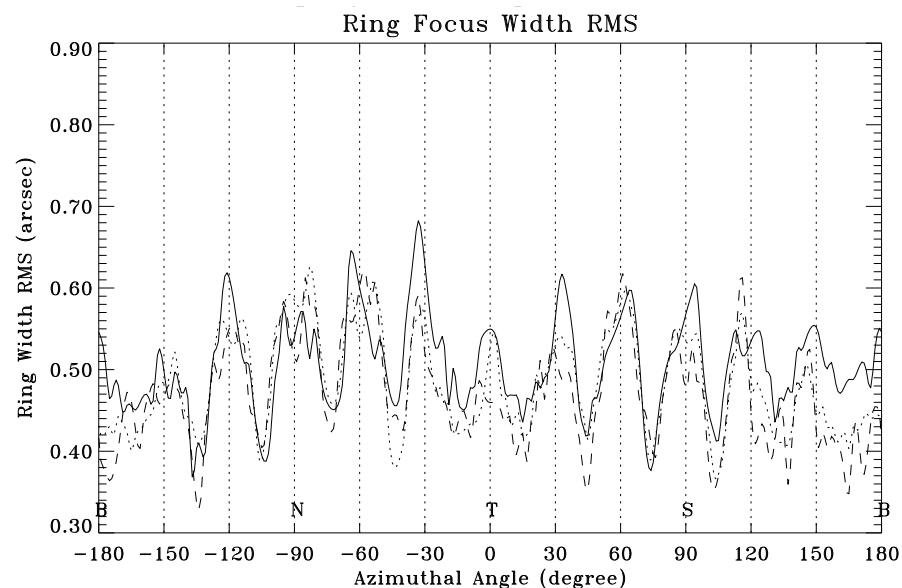


Figure 18.26: The Ring width RMS for ring 6, from three ring focus measurements on 1996/12/23, 1997/02/10 and 1997/04/10.

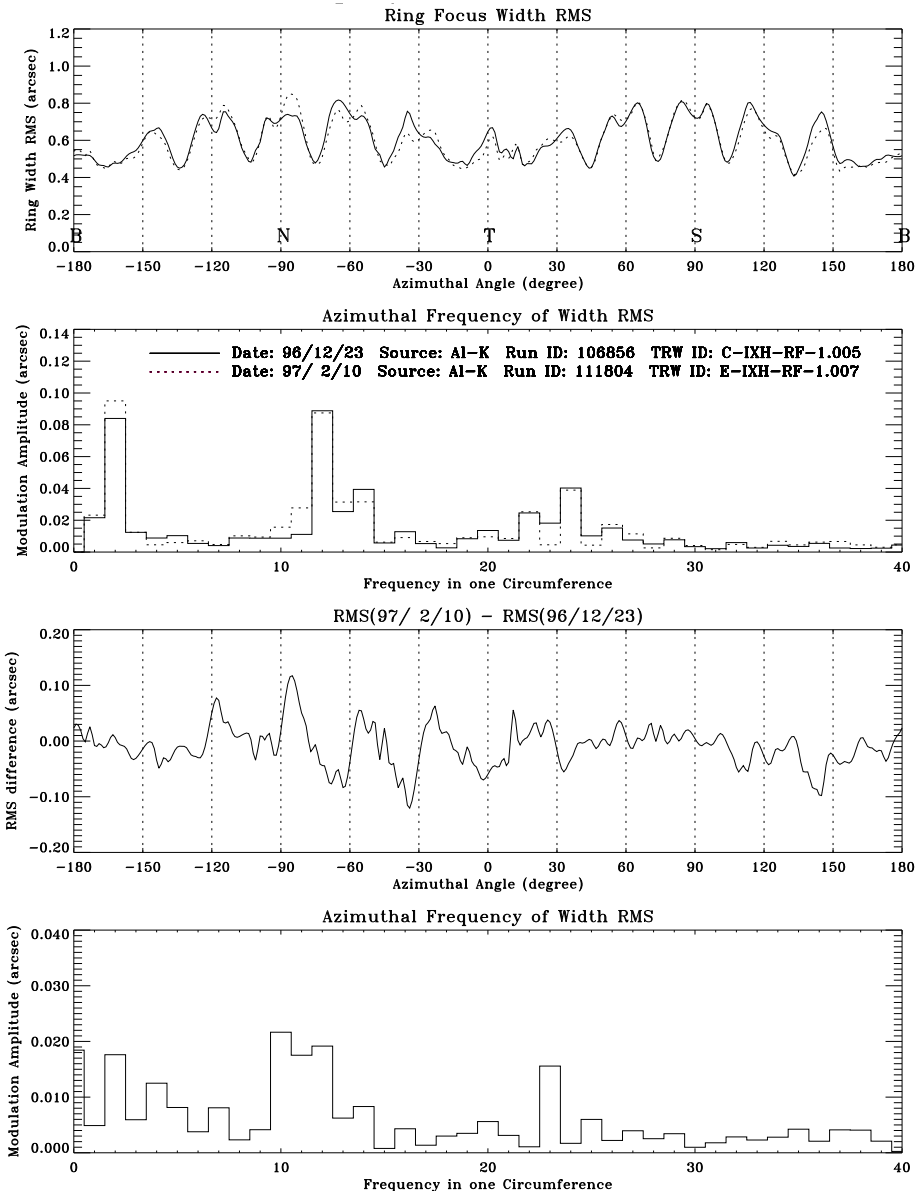


Figure 18.27: HRMA ring focus Data: Ring 1, Al-K source, data of 1996/12/23 and 1997/02/10 and their difference.

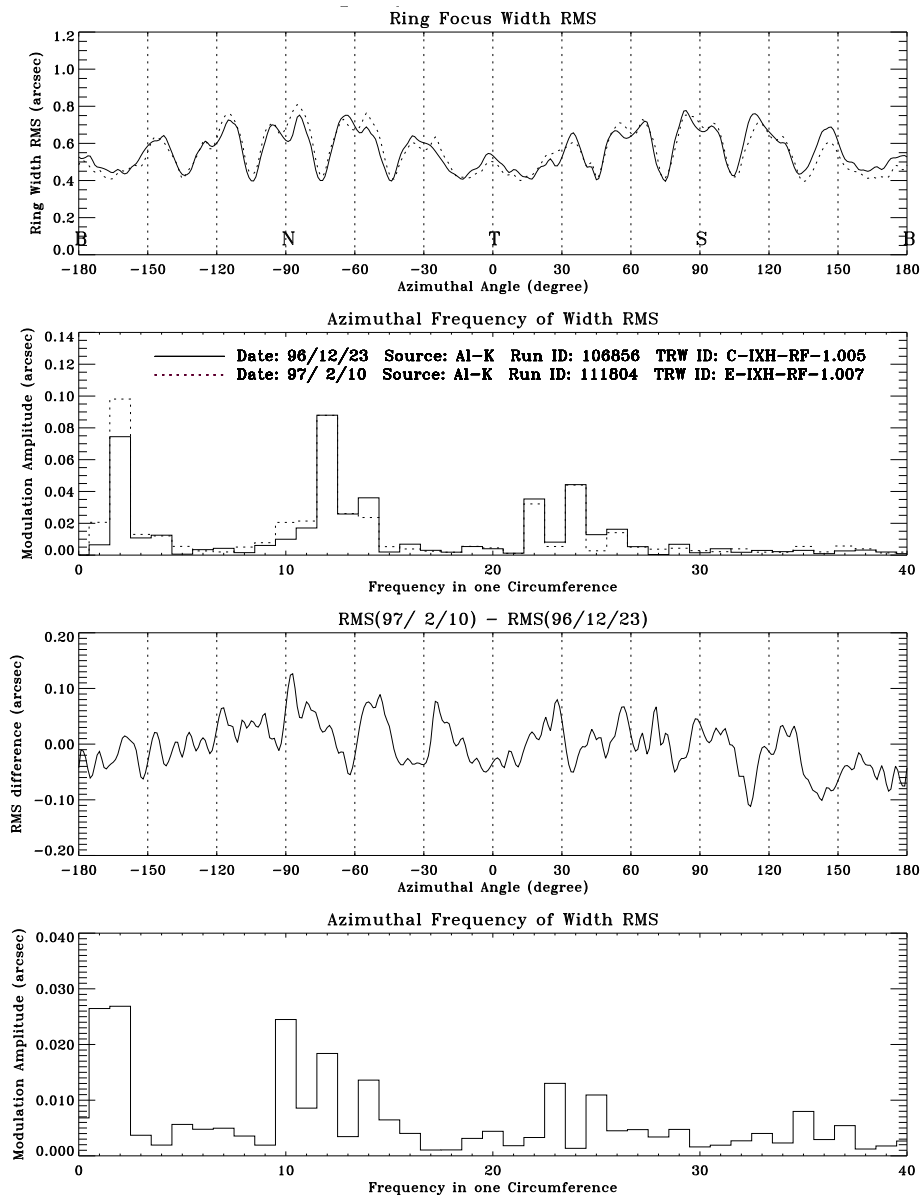


Figure 18.28: HRMA ring focus Data: Ring 3, Al-K source, data of 1996/12/23 and 1997/02/10 and their difference.

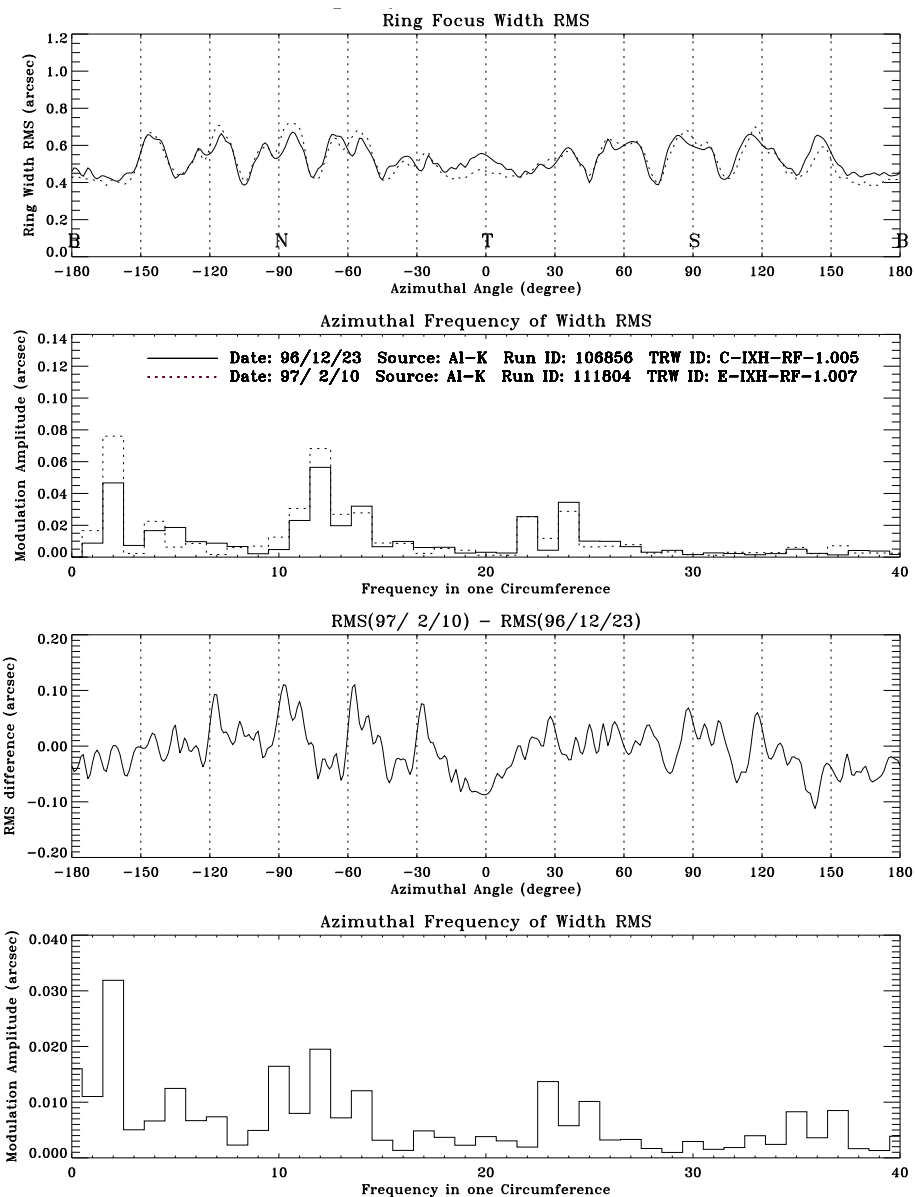


Figure 18.29: HRMA ring focus Data: Ring 4, Al-K source, data of 1996/12/23 and 1997/02/10 and their difference.

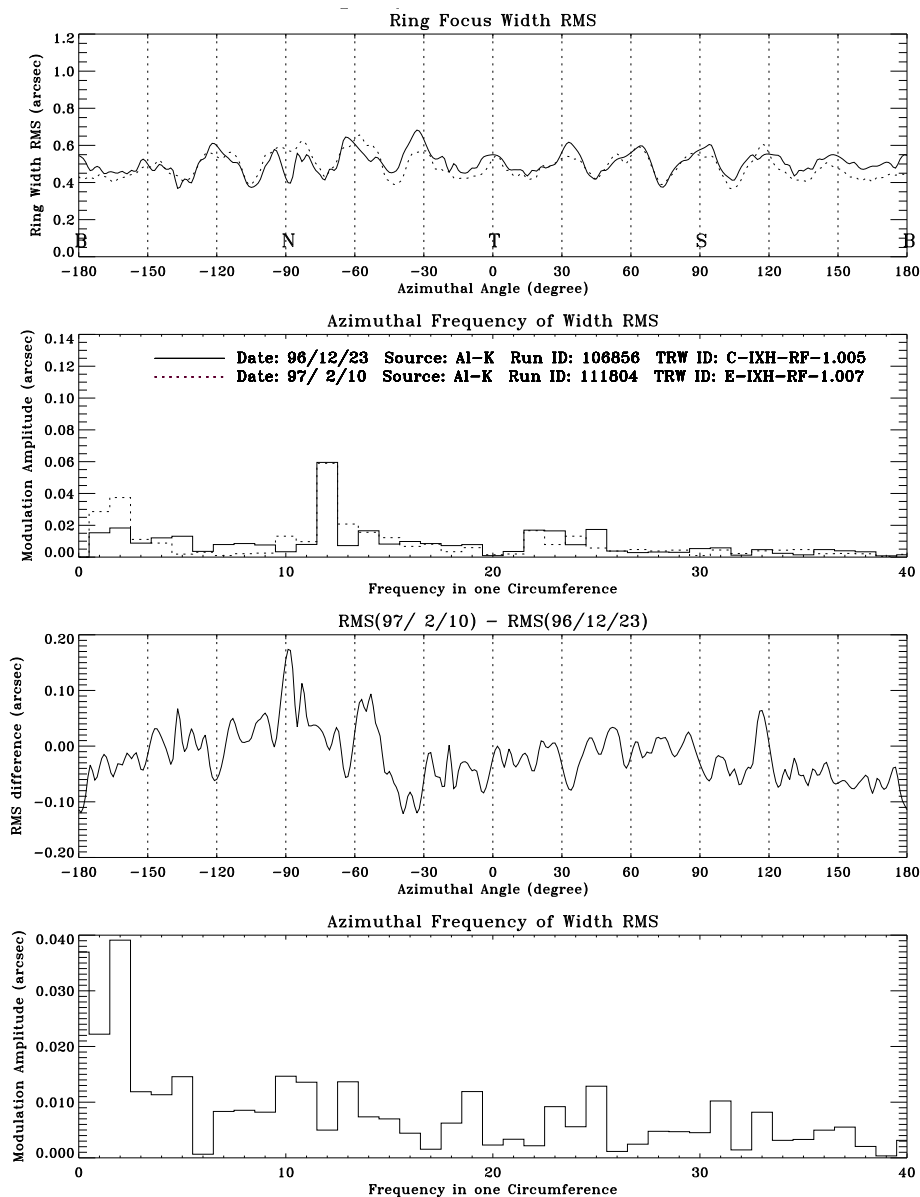


Figure 18.30: HRMA ring focus Data: Ring 6, Al-K source, data of 1996/12/23 and 1997/02/10 and their difference.

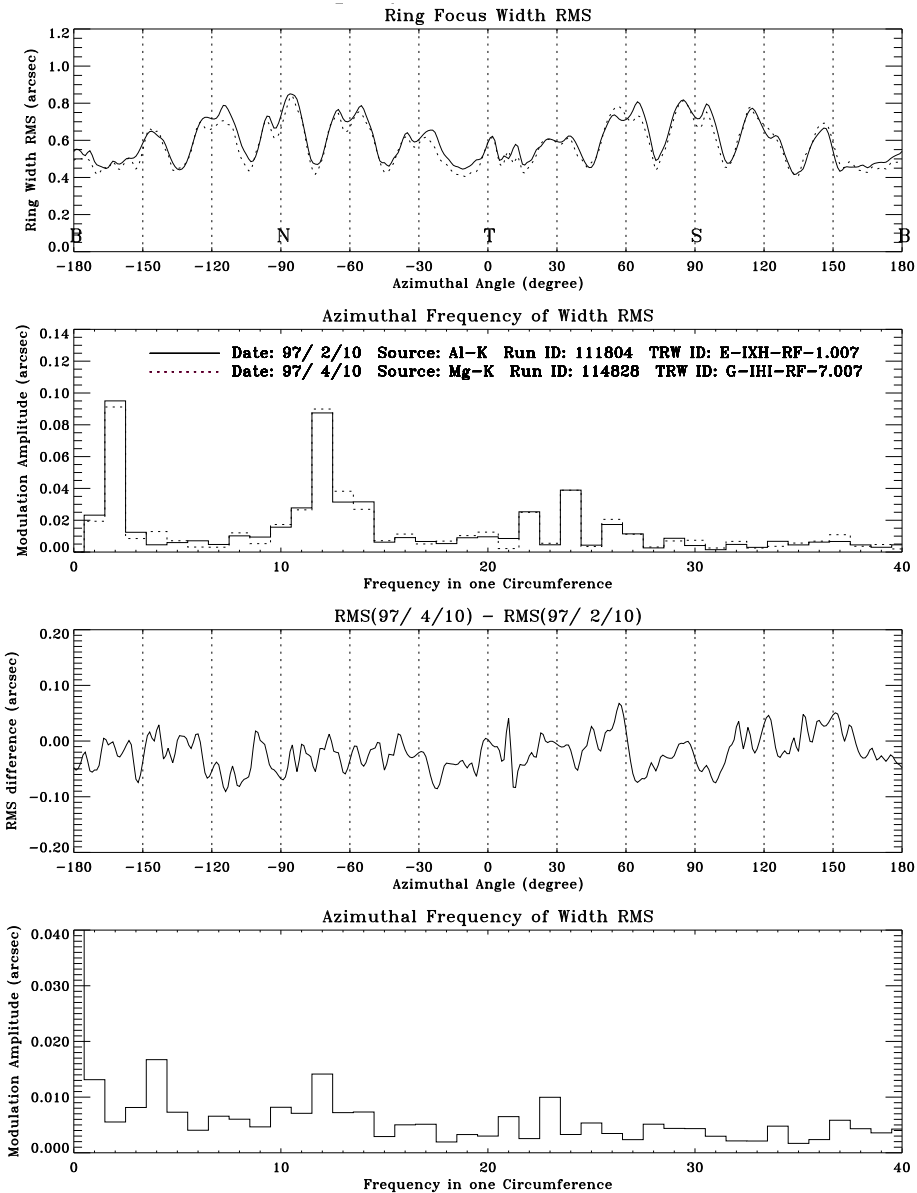


Figure 18.31: HRMA ring focus Data: Ring 1, Al-K source, data of 1997/02/10 and 1997/04/10 and their difference.

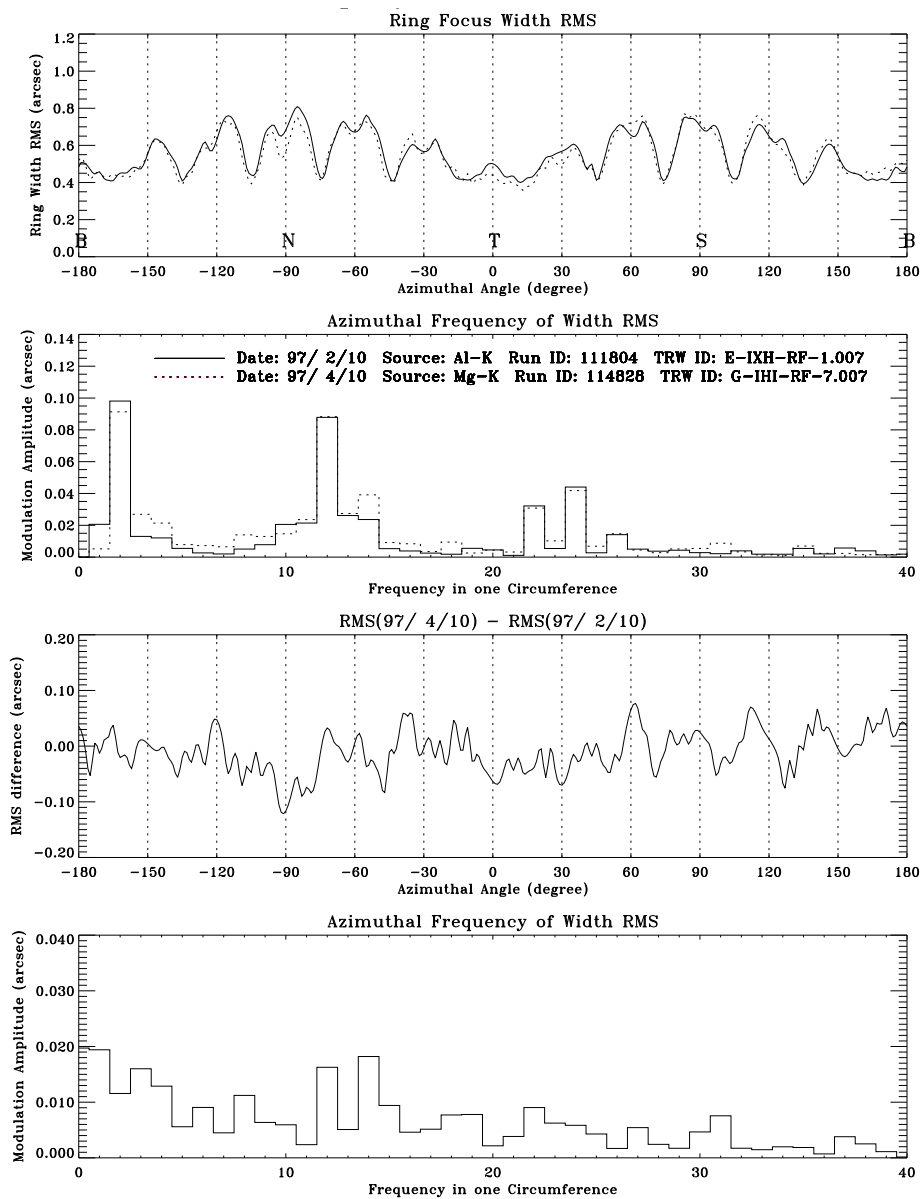


Figure 18.32: HRMA ring focus Data: Ring 3, Al-K source, data of 1997/02/10 and 1997/04/10 and their difference.

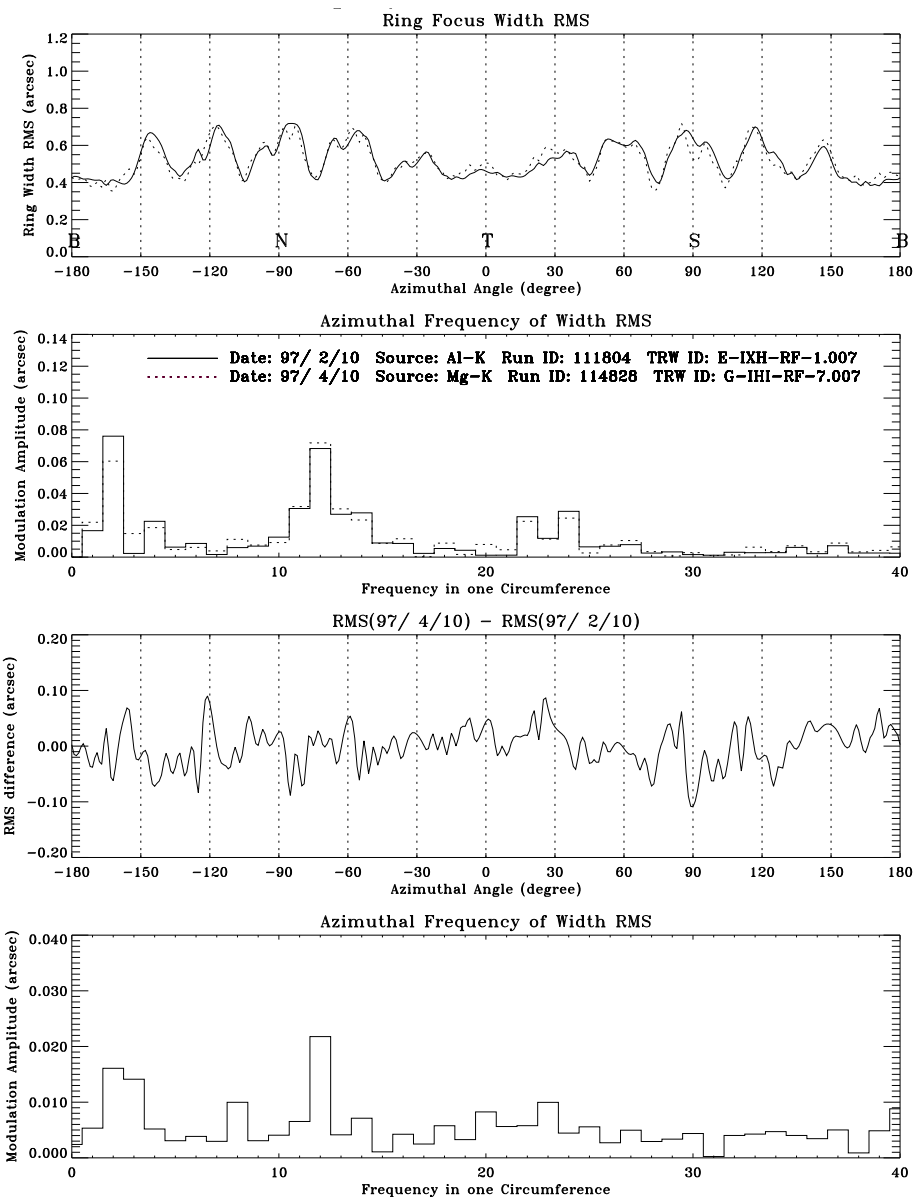


Figure 18.33: HRMA ring focus Data: Ring 4, Al-K source, data of 1997/02/10 and 1997/04/10 and their difference.

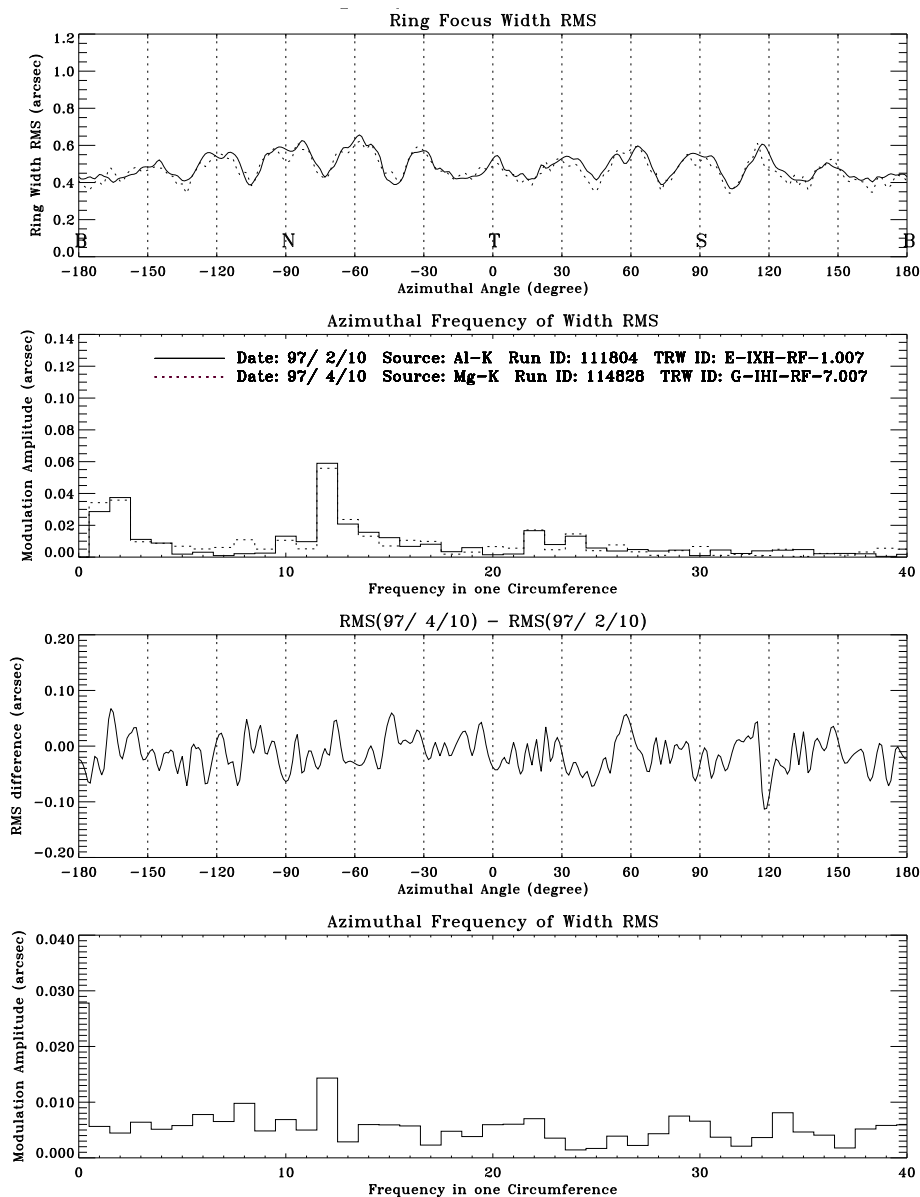


Figure 18.34: HRMA ring focus Data: Ring 6, Al-K source, data of 1997/02/10 and 1997/04/10 and their difference.

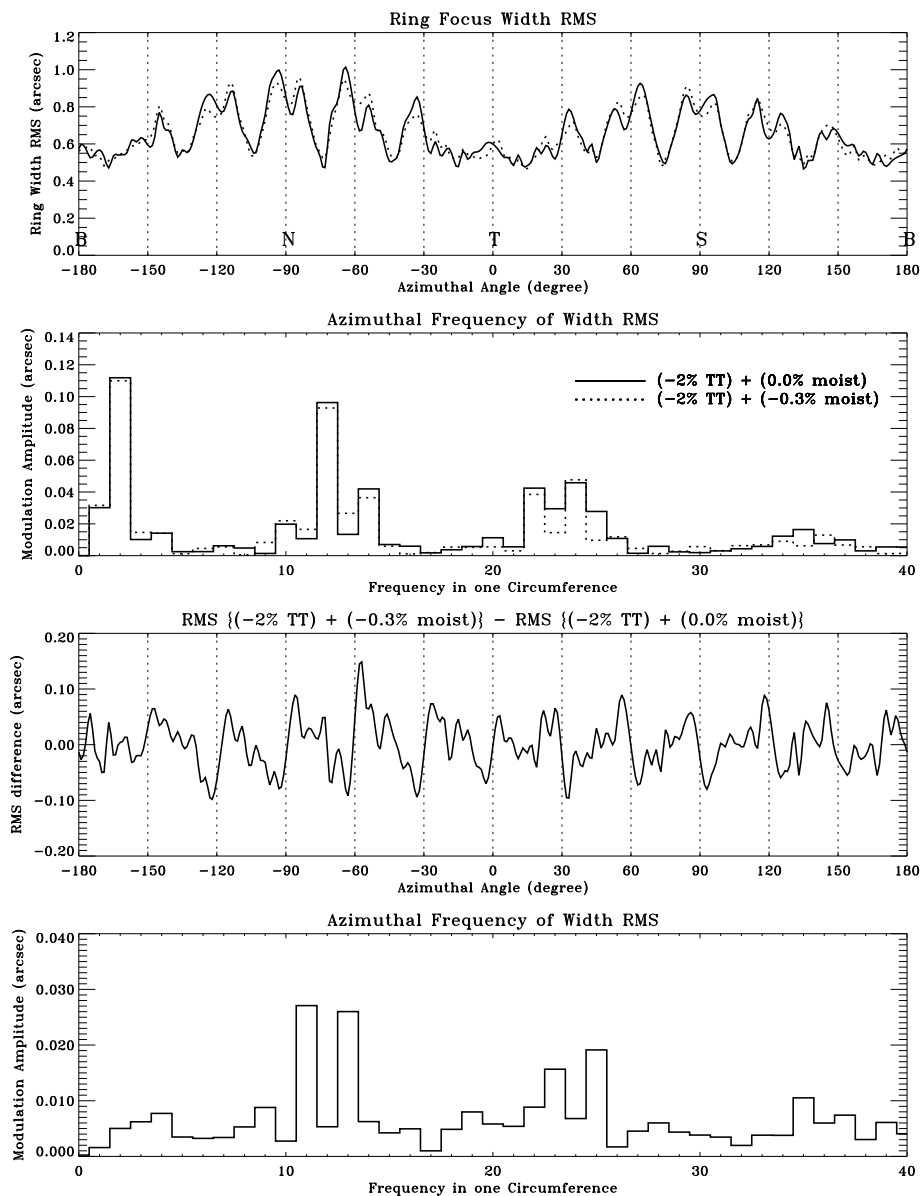


Figure 18.35: HRMA ring focus model: Ring 1, Al-K source, epoxy strain with 0.0% and -0.3% moist and their difference.